DESIGN AND FABRICATION OF SIMPLE MICROSTRUCTURES FOR BIOMEDICAL APPLICATIONS USING TWO-PHOTON FEMTOSECOND 3D LIGHT-FIELD LITHOGRAPHY

A Thesis

by

BALAJI BASKAR

Submitted to the Graduate and Professional School of
Texas A&M University
in partial fulfillment of the requirements for the degree of

MASTER OF SCIENCE

Chair of Committee,	Sy-Bor Wen
Committee Members,	N.K. Anand
	Sheng-Jen Hsieh
Head of Department,	Guillermo Aguilar

May 2022

Major Subject: Mechanical Engineering

ABSTRACT

Micro and nanofabrication techniques have revolutionized medical and pharmaceutical industries by their ability to mass fabricate biomedical devices with complex functionalities and geometries. 3D microsystems have significant advantages over 2D microsystems in better optical, electrical, mechanical, and biological properties in a much compact domain. Conventional 3D microstructures are fabricated by layer-by-layer stacking 2D fabrications, also known as 2.5D fabrication (micro stereolithography, micro laser sintering, electron beam lithography, etc.), or by direct 3D fabrication (holographic lithography, single spot multiphoton lithography). But these techniques have few or more limitations based on the type of fabrication materials, cost, process time, experimental setup constraints, and final resolution. For a fast throughput 3D microfabrication with good spatial resolution, this study proposes a new photolithography technique based on 3D light-field imaging principles. 3D light field projection is achieved with a spatial light modulator and a microlens array to direct light-rays to designed voxel positions in 3D space. Femtosecond light of high intensity is chosen as the light source for such precise microfabrication. Unlike single-photon absorption in UV light which causes unwilling curing of resists along the optical path, femtosecond light rays can accurately cure designed focal spots in 3D space through two-photon absorption. Due to the premature intersection of light rays before arriving at a voxel location, unwanted voxels are generated, which causes a mismatch between designed and fabricated microstructures. This thesis work mainly focuses on addressing this issue by improving the voxel generation algorithm to reduce unexpected voxels and ensure accurate high-speed patterning of simple microstructures with potential applications in biomedical sciences.

ACKNOWLEDGEMENTS

I would like to thank my committee chair, Dr. Sy-Bor Wen, for his guidance and support throughout my thesis research. I would also like to thank my committee members, Dr. Anand Nagamangala, and Dr. Sheng-Jen Hsieh, for their valuable guidance.

I want to thank my colleague Aravind Jakkinapalli for the valuable discussion and constant support throughout my research. I would also like to thank my other colleagues from the lab Hongjie Zhang, Arun Bhaskar, and Ke Li, for their valuable support. Also, I would like to thank Dr. Yakovlev and his group for their technical support on laser usage.

Finally, I would like to thank my parents and sister for their encouragement and support.

CONTRIBUTORS AND FUNDING SOURCES

Contributors

This work was supported by a thesis committee consisting of Professor Sy-Bor Wen and Professor Anand Nagamangala of the Department of Mechanical Engineering and Professor Sheng-Jen Hsieh of the Department of Engineering Technology and Industrial Distribution.

All work for the thesis was completed by the student, under the advisement of Professor Sy-Bor Wen of the Department of Mechanical Engineering.

Funding Sources

This work was supported by National Science Foundation (CMMI – 1826078). Graduate study was supported by Graduate Fellowship and Summer Graduate Research Assistantship from the J. Mike Walker’66 Department of Mechanical Engineering at Texas A&M University.

TABLE OF CONTENTS

Page

LIST OF FIGURES

LIST OF TABLES

Page

1. INTRODUCTION

The vast demand for miniaturization of products in the electronics and biomedical industries has paved the way for several microfabrication techniques. Microfabrication uses integrated circuit manufacturing technology and other processes to fabricate structures in the micrometer to even nanometer scale. 3D microstructures are becoming more valuable in industries due to their compact size and better mechanical, electrical, optical, and biological properties over 2D microstructures [1]. 3D microstructures also have several advantages like small size, high surface area to volume ratio, integrable with electronics, usage of small sample volumes, high throughput, easy batch processing, and precise geometry control. [2]

Apart from electronics, microfabrication has many applications in medicine and biology, categorized into four major domains, tools for biochemistry and molecular biology, medical devices, tissue engineering, and biosensors [3]. 3D microscale fabrication methods have emerged as powerful tissue engineering tools [4] and micro drug delivery mechanisms [5]. The main biomedical application in tissue engineering is the fabrication of 3D micro scaffolds, which act as templates for cell aggregate formation in a spatially regulated manner. Injuries and diseases can cause damage to the existing tissues in living organisms which creates a huge demand for artificially grown tissues to be transplanted into the affected organism [6]. This makes tissue engineering one of the vital growing fields which involve fabricating an artificial 3D environment that can mimic a living organism interface where cells can grow controllably and form tissues. The 3D structure is manipulated for cell growth based on the resolution of fabrication and biocompatibility of the material used for fabrication. By altering the physical and chemical properties of the polymer material being used, the organ's final shape, including the proliferation rate of the cells on these structures, can be selectively controlled [7]. Tissue engineering is an interdisciplinary field of science that involves cell therapy and 3D manufacturing methodologies. The adult stem cells, capable of growing and differentiating into any tissues and organs, are made to grow *in vitro,* in a 3D environment that can closely mimic the natural tissues. Such artificial organs and tissues can be transplanted later into the organism. In some cases, the fabricated 3D scaffold is directly transplanted *in vivo* into the organism, and the biological tissues are formed on this interface using the body's natural forces. In either of these cases, the cellular and physiological interactions of these tissues with the artificially created 3D scaffolds will depend on the material used and the process parameters of that micro or nanofabrication techniques [8]. One such application of DMD-based UV stereolithography in fabricating 3D human tissue constructs is shown in *Figure* 1.

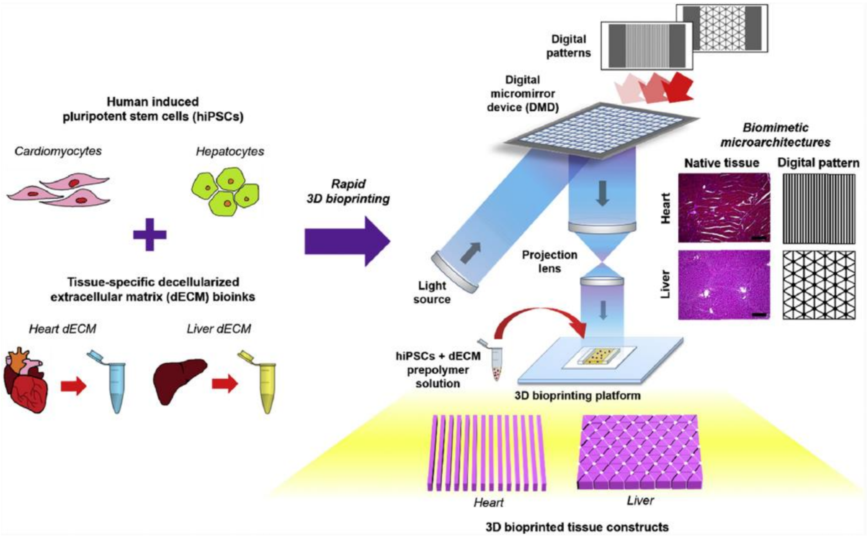

Figure 1: Overview of a 3D micro bio fabrication technique to fabricate tissue constructs with tissue-specific stem cells. Human-induced pluripotent stem cells are combined with their respective tissue-specific photocrosslinkable decellularized extracellular matrix (dECM) bioinks. Parallelly, digital

patterns capturing the histological features of heart and liver tissues were fabricated by a DMD-based 3D micro stereolithography process. The cell solution is later added to fabricate tissue constructs having biomimetic microarchitecture. Reprinted from [9].

Another important application is the fabrication of 3D micro-drug delivery devices. Advances in micro and nanofabrication technologies changed the way of drug delivery and enabled the manufacturing of devices to deliver drugs precisely to the target regions [10]. The type of micromanufacturing method allows for precise control over surface topography, feature size, and biocompatibility of the material with the carrier drug. There are several routes for drug delivery, including oral drug delivery, transdermal drug delivery, direct implantable devices, etc. [11], which invokes several microfabrication techniques to fabricate these microdevices. One such application for transdermal drug delivery is shown in *Figure 2*.

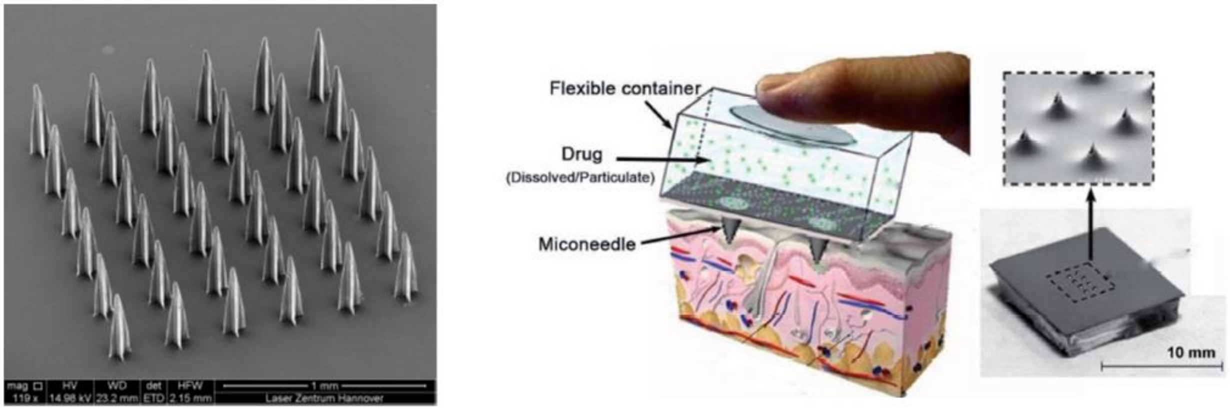

Figure 2: Microneedle-like structures (10 μm x 5 μm) fabricated using femtosecond multi-spot multiphoton lithography. The working mechanism of a transdermal drug delivery device. A small flexible container with the drug can be stuck to the skin like a patch to initiate drug delivery. Reprinted from [12].

Transdermal relates to drugs injected through the skin using an adhesive patch which is slowly absorbed by the body. Microneedle-mediated drug delivery is an advanced technique for the transdermal delivery of proteins, insulin, and other pharmacologic agents to treat various diseases [11]. These are primitive needle-shaped microstructures that can be fabricated by various techniques. Overall, with everyday innovation, basic MEMS and NEMS 3D fabrication techniques initially developed for the electronics industry also have a wide range of applications in the biomedical sciences. In the following subsection, we will review some of the common 3D microfabrication methods.

1.1. Review of current 3D microfabrication techniques

Microscale structures and devices are fabricated by several techniques adopted from the semiconductors field or developed explicitly for microfabrication. The desired microstructures can be built within the bulk of the substrate (bulk micromachining) or on the surface of the substrate (surface micromachining), or a combination of both. The essential microfabrication techniques pertaining to medicine are film deposition, etching, bonding, and lithography [13]. Film deposition involves the deposition and formation of micron-thick films on the substrate surface[13]. On the other hand, etching selectively removes materials from thick substrates by either physical or chemical processes [13]. Bonding adheres two substrates together without using intermediate layers in between [13]. However, these three techniques have become obsolete and broadly replaced by modern-day lithography and other microfabrication methods.

Lithography is the process of writing 2D and 3D patterns on a substrate. The name is originally derived from Greek words meaning writing on stones, which in the fabrication world means using light to write patterns on a substrate like Si through a light-sensitive photo material. There are different lithography-based micro and nanofabrication techniques to produce 3D structures. However, all these techniques have some limitations regarding materials used, experimental constraints, resolution, and complexity of the fabricated structure. Some lithography methods like UV stereolithography, X-Ray Lithography, electron beam lithography, etc., can fabricate 3D micro and nanostructures through layer-by-layer stacking of 2D fabrications, also known as 2.5D fabrication. Some micro and nanofabrication lithography techniques like holographic and single spot multiphoton lithography are used to fabricate 3D structures directly without the need for layer-by-layer stacking of 2D structures [14]

X-ray lithography is a promising micromachining technique that can fabricate micro and even nanostructures with high aspect ratios. It is often combined with a metal electroplating process to be used as mold inserts. This sequential process is known as LIGA, a German abbreviation for Lithographie, Galvanoformung, and Abformung. The Deep X-ray – LIGA process can produce microstructures in polymers like PMMA using X-ray masks fabricated by conventional UV lithography [15]. The process involves depositing polymer like PMMA on a primary substrate, exposing it to columnated X-rays through an intermediate X-ray mask and developing, electrodepositing metal on the substrate, and removing PMMA to form free-standing metal structures. These free-standing structures can be the final product or can be used as molds to mass replicate these structures using injection molding. In deep X-ray lithography, an X-ray mask of thickness 20 μm is used to block deep X-rays, which causes the back-scattering effect. By imposing a two-step dose distribution on the PMMA with and without the X-ray mask, tapered 3D micropillars with a gap size of 40 μm and aspect ratio of over 7 with pillar size of 130 μm and pillar height of 930 μm were achieved [16]. UV light is used to produce relatively lower aspect ratio structures to reduce the investment costs for synchrotrons. UV-LIGA process was used to fabricate highly accurate sub-THz 3D waveguides [17] and micro electromagnetic relay for power applications [18] by stacking and spin coating multiple thin layers of SU-8 photoresist to provide improved planarity and surface quality. The main challenge of the X-ray - LIGA process is to produce high-energy X-rays with synchrotron. X-ray masks used during exposure are expensive to produce, making the cost of the process high [19].

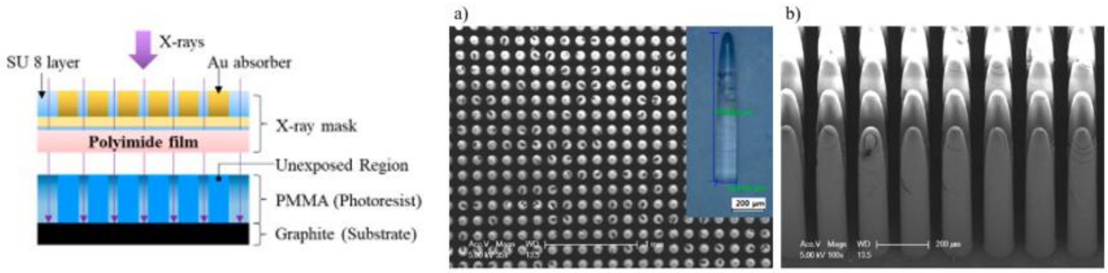

Figure 3: a) Deep X-ray lithography with an X-ray mask. X-ray mask is fabricated by UV lithography and by electroplating Au. PMMA photoresist is exposed by unblocked deep X-ray irradiation to form 3D micropillar structures. b) Tapered micropillar structures have an aspect ratio of over 7 with a pillar size of 130 μm and pillar height of 930 μm. Reprinted from [16]

For fabrication of extremely small two-dimensional structures, sub-diffraction limit of around 2 nm – 10 nm, electron beam lithography (EBL) technique is used where a narrow beam of high energy electrons (~ 10 – 100 keV) is scanned in a sequential pattern across a substrate covered with photoresist sensitive to electrons [20]. The resists are polymeric electron beam sensitive substances like PMMA, where the exposed regions undergo chemical modification with a different solubility than the unexposed regions. The electron gun source can be field emission for higher resolution or thermionic emission for low resolution [21]. Although electron beam lithography effectively fabricates high-resolution two-dimensional nanostructures, it is not feasible to realize 3D nanostructures by stacking the 2D nanostructures because it is difficult to control the overlay alignment errors while stacking these 2D nanostructures in a nanoscale [22]. However, few groups have recently tried to make the 3D electron beam lithography feasible through ice lithography technology. In this method, thin water or organic ice films or resists are patterned by a focused electron beam [23]. This method can produce high aspect ratio nanostructures around 15, with a minimum line width of 20 nm over a 300 nm thick ice resist layer. The production throughput of iEBL for a beam current of 100 pA is 0.12 μm^2/min [24]. iEBL also allows for dose modulated exposure of electron beams that selectively cures and removes different parts of the ice resist. This allows iEBL to carefully fabricate 3D nanostructures within each layer by designing the dosage distribution [24]. The alignment process is necessary for 3D nanofabrication for overlaying previously fabricated layers. This is done by fabricating alignment marks along with the first fabricated 2D structure, which acts as reference coordinates for the subsequent layers. These alignment errors are usually high for EBL resist like PMMA, where SEM imaging could expose the fabricated structures. Water ice, less sensitive to electron beam exposure, can recognize previously fabricated structures, making them good alignment marks. However, the low sensitivity of water ice leads to more exposure dose (almost three times that of PMMA) for fabricating, which makes iEBL a slow process [23]. Also, the backscattered primary and secondary electrons can significantly reduce the resolution of electron beam lithography (proximity effect). The requirement of vacuum in electron generation source also increases the cost of the system [25].

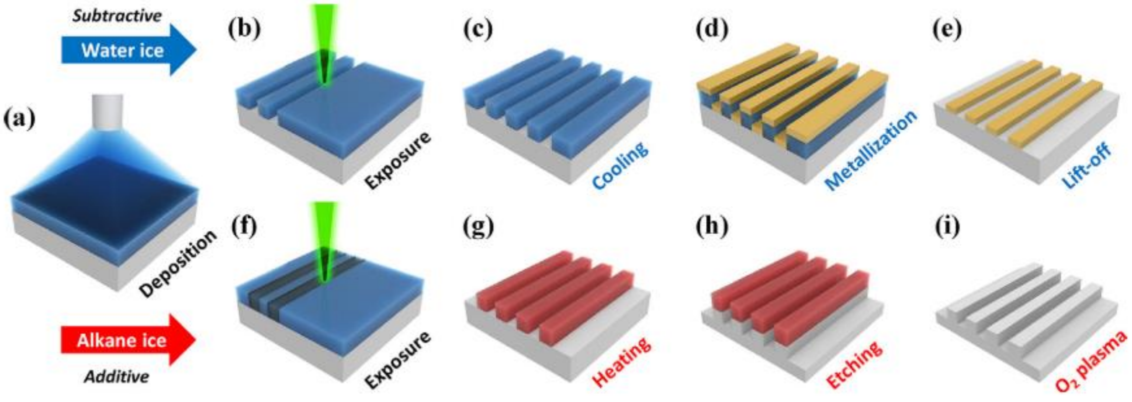

Figure 4: Process flow in a typical ice electron beam lithography for water ice positive resists (a – e) and alkane ice negative resists (f – i). Reprinted from [23].

Micro stereolithography (μSLA) is a layer-by-layer 3D fabrication method based on photopolymerization of liquid photo-sensitive polymers/resins. The 3D object to be fabricated is divided into several single cross-sectional layers by slicing the standard tessellation language (STL) file. Stereolithography has undergone several modifications over the years, and it can be broadly classified into four generations [26]. The earliest or the first generation is known as scanning stereolithography. In this method, a scanning UV light source polymerizes the photopolymers through single-photon polymerization. Scanning is achieved by using galvanometric mirrors to move along the X-Y direction [27]. However, using mirrors can cause the light to defocus with some optical errors.

The focused UV light spot is fixed on the resin and is translated by a separate X-Y translation stage. A typical scanning stereolithography system contains a UV light source, vat containing liquid prepolymer, height-adjustable sample platform, x-y stage controlled by a computer [26]. The platform holding the sample moves downwards by a distance equal to the vertical resolution, which could be as small as 0.1 μm, which forms the thickness of each layer [28]. This method usually takes long fabrication times due to point-by-point scanning. The fabrication time can be improved by the second-generation methods, known as projection stereolithography. In this method, each layer of a 3D object can be printed directly with a single exposure by inserting a dynamic mask into the system. A digital micromirror device (DMD) or a Liquid Crystals on Silicon (LCOS) chip is used as the dynamic mask where each 2D slice is transferred to the chip as a bitmap image [28], [29]. As opposed to the laser beam's point-by-point scanning, the entire 2D slice can be projected with DMD, where multiple pixels on the DMD can send light to different locations on the photopolymer. A dynamic mask can precisely control the exposure time and provide a good resolution of around 5 μm and layer thickness of around 1 – 10 μm [28]. The fabrication time of projection stereolithography methods can be improved by third-generation methods known as continuous stereolithography. Although projection lithography allows us to fabricate each layer quickly with a single exposure, the process is not continuous from layer to layer. For each layer, the resin is cured by UV light which is mechanically moved outside the resin surface, and the system is repositioned for the next layer. These sequential steps take several seconds, which restricts the printing speed of the system to a few millimeters per hour. This is overcome by a recently proposed method known as Continuous Liquid Interface Production (CLIP) in the third generation. In this process, a liquid interface known as the dead zone with an oxygen-permeable window is set up below the UV projection plane to fabricate structures without stops from layer to layer. The dead zone inhibits photopolymerization between the polymerizing part and window, which allows the part to be continuously cured during vertical movement [30]. With this method, the printing speed was improved up to hundreds of millimeters per hour with a resolution of around 5 μm [31]. One major limitation with these three generations is that there is a restriction on the choice of materials that can be used as liquid photopolymer resins. Also, support structures are required for stereolithography to securely attach the fabricated part to the print head and avoid warping. Support structures used in SLA are thin with good contact to the part, making the removal process hard. Removing the support framework can leave marks on the fabricated part that need to be polished to ensure a good surface finish [32]. The last or the most recent generation, known as volumetric stereolithography, was proposed to overcome these difficulties. Like holographic lithography, this process can directly fabricate 3D objects as a unit operation. One such promising method is tomographic volumetric stereolithography, where the entire volume of the liquid resin is simultaneously irradiated. A cylindrical container containing the resin is rotated and irradiated on the sides by computed patterns of light [33]. The resin is exposed from all angles by the patterns, and a 3D accumulation of light dose on the resin cures the whole resin to form 3D objects. This method can produce complex 3D parts with a wide range of materials and a high throughput or printing speed up to 10^5 millimeters per hour. However, the resolution of the system is restricted from 80 μm to 300 μm [33].

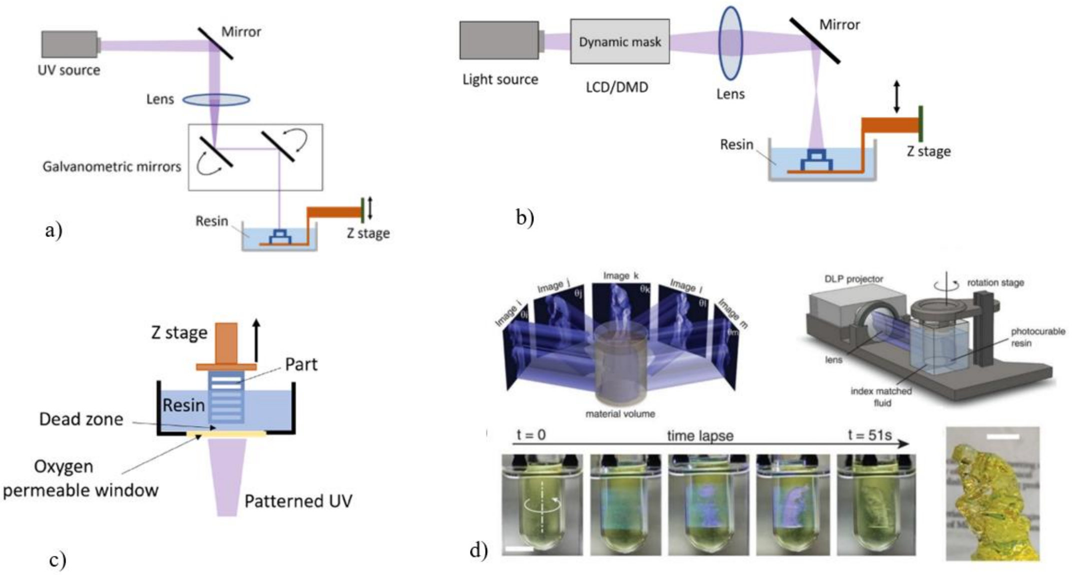

Figure 5: The four generations of UV stereolithography. a) schematic of a scanning stereolithography b) schematic of projection stereolithography with a dynamic mask c) schematic of Continuous Liquid Interface Production (CLIP) stereolithography d) Experimental procedure for tomographic volumetric stereolithography. Reprinted from [26]

Selective laser sintering (SLS) is a powder metallurgy technique initially developed for casting patterns from plastic powder. It is not a lithography-based method, but it is widely used for microfabrication. Typically, a high-energy laser beam like continuous wave CO_2 laser-focused down to 50 – 300 μm beam spot size is scanned over a bed surface filled with metal powders and selectively sinters the surface of the powder bed [34]. High energy laser fuses the powder to form a solid part based on the designed pattern. After one pass of the laser scan, the bed is lowered, and the loose powder is pushed out. A fresh even layer of powder is applied to the bed using a roller, and the next layer is fabricated similarly until the desired 3D structure is fabricated [35]. In an SLS process, no support structures are required in fabricating complex free-standing structures since the loose powder supports the 3D part on the bed as the bed moves down sequentially. A variant of this method is called Selective Laser Melting (SLM). Even higher laser beam intensities increase the temperature sufficiently to melt powders into the liquid phase [34]. Materials used include metal powders (Ag, Al, Cu, Mob, Stainless steel), polymers, and ceramics (alumina, silicon carbide). Micro selective laser sintering (μSLS) is a modified process that can improve the resolution of fabricated structures down to 10 μm range [36]. The resolution could be further enhanced by using sub-micron-sized powders to fabricate ceramic and metallic microstructures. The currently achievable resolutions with this method lie in the range of 10 – 50 μm with a minimum layer thickness of 1 μm and aspect ratio (height/width) of 1:25 [37]. Recently a novel microscale selective laser sintering process was used to fabricate metal parts with sub 5 μm resolution and a throughput of around 60 mm^3/hour [38]. The surface finish of the microstructures is coarse, with a surface roughness of ~ 35 μm. One reason is that the compactness of powder reduces as the powder size becomes smaller, resulting in limited heat conduction, reduced wetting between particles, and reduced density of laser-sintered material. Another reason is that the expanding plasma plume during laser irradiation can push the melting locally downwards, causing an undulation on the surface, also known as the condensing effect [34]. Smaller-sized powders (< 2 μm) react more actively with oxygen and humidity to form agglomerates causing huge exothermic reactions. A significant limitation of this method is to develop an oxygen-free vacuum environment with special powder handling methods to ensure the fabrication of microstructures with good structural integrity and a higher density of sintered material [39].

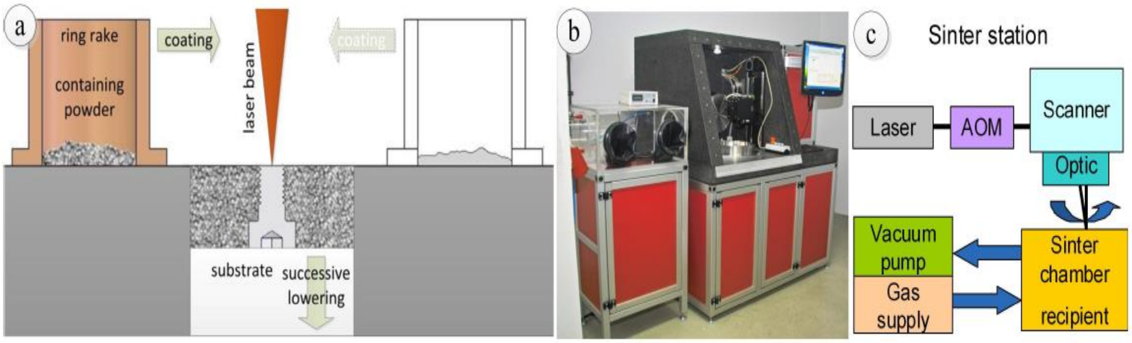

Figure 6: a) Schematic description of a typical selective laser micro sintering process. The powder is transported and coated by a ring rake cylinder attached to a piston. A focused laser beam is used to sinter the powder particles. b) Developed laser micro sintering station c) Schematic view of the station with all the main components like the laser, acousto optic modulator, vacuum system, main optical system, and gas supply system. Reprinted from [34]

Multiphoton lithography is a direct 3D fabrication method where high intensity near IR laser beams can cure desired spots by two-photon or multiphoton polymerization. This method relies on multiphoton absorption in a material that is transparent to the fundamental wavelength of the laser. Single spot multiphoton lithography is a high-quality 3D microfabrication technique that allows us to produce features smaller than the diffraction limit [40]. However, this approach of point-by-point scanning in 3D volume requires precise galvanometric mirrors and can take a long time to fabricate structures with complex geometries. The fabrication time could be improved by implementing multi-spots multiphoton lithography. However, using multiple laser foci simultaneously at different regions using a stage scanning system will form identical features at all focal positions resulting in periodic patterns [41].

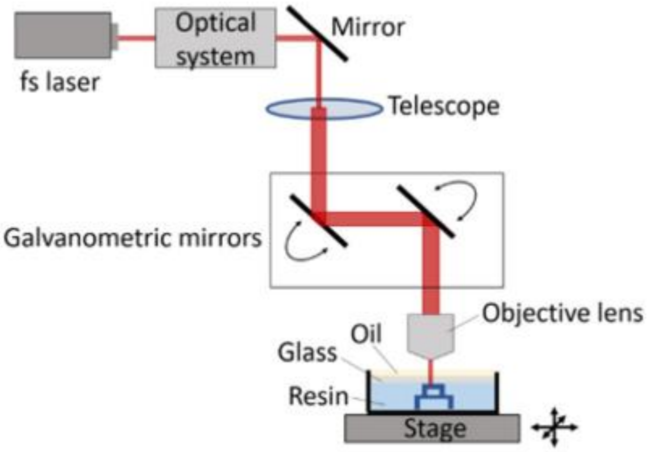

Figure 7: Schematic setup of a typical single spot multiphoton lithography implemented with femtosecond laser source. Reprinted from [26].

Holographic lithography is a fast process to fabricate 3D structures directly without the need for x-y stages. In holographic lithography, the information of a 3D object is digitally created using a computer (computer-generated holograms) or optically generated by recording interference between a coherent reference beam and a diffracted beam from the object and storing it in a crystal or a film. Optically, the hologram is reconstructed by illuminating the film with a coherent wave plane to obtain the 3D object [42], whereas a computer-generated hologram displays the 3D object slice by slice digitally by fresnel propagation along the optical axis [43]. The direct writing speed of holographic lithography is ~ 10^8 $\mu m^3/s$ for a 10 mm coherent laser beam which is significantly higher than the prolonged writing rate ~ < 10^3 $\mu m^3/s$ of two-photon polymerization method [44]. Although holography captures the phase information (depth) of a 3D object, fabrication is restricted to the outer surfaces of the 3D object, which may cause insufficient curing to the inner regions [42]. The coherent reference beam causes a lot of speckles in the interference pattern, reducing the quality of the final 3D output [45]. The system constantly has alignment issues and needs to be kept very stable. Even a slight movement in the optics can destroy the interference fringes, which contain both phase and intensity information of the 3D object.

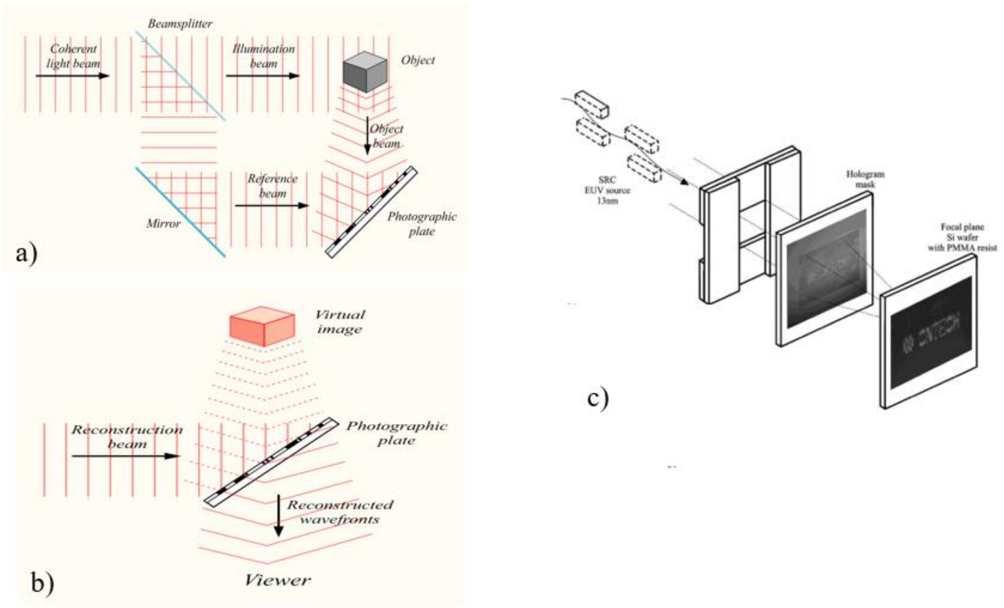

Figure 8: Principle of holography a) The process of recording the interference between a reference beam and an object beam to form a hologram b) The process of reconstructing the original object by illuminating the hologram with a reconstructing beam c) Experimental setup of holographic lithography technique using extreme UV radiation. Reprinted from [42]

Table 1: Summary of different micro and nanofabrication techniques

Method	**Spatial resolution**	**Fabrication speed**	**Layer by layer fabrication**	**Scanning in XY direction**
Stereolithography	< 5 μm	$\sim 10^5$ μm^3/s	Yes	Yes
Selective laser sintering	< 5 μm	$\sim 1.6 \times 10^7$ μm^3/s	Yes	Yes
Electron beam lithography	< 5 nm	$\sim 10^2$ μm^3/s	Yes	Yes
X-ray lithography	< 50 nm	$\sim 10^2$ μm^3/s	Yes	Yes
Single spot multiphoton lithography	< 100 nm	$\sim 10^3$ μm^3/s	No	Yes
Holographic lithography	> 1 μm	10^8 μm^3/s	No	No

1.2. Motivation

From the review of current 3D microfabrication methods as summarized in Table 1, there is a requirement for high-resolution 3D fabrication with high throughput. Although single spot multiphoton lithography provides a very high spatial resolution and can form spots directly in 3D space, the point-by-point serial approach increases the fabrication time. Even in the case of projection stereolithography, 2D structures could be patterned in a single projection, but to form 3D structures, layer by layer scanning will also increase the fabrication time. So it is required to pattern 3D structures in a single projection without point-by-point scanning or layer-by-layer stacking to have high throughput, as in holographic lithography. However, the requirement of a coherent laser beam for holography inevitably forms speckles that result in poor resolution. Hence for any proposed 3D microfabrication method, a good balance between spatial resolution and throughput must be achieved

In this study, a 3D photolithography technique based on light field imaging principles is proposed. In this method, a Microlens Array (MLA) and spatial light modulation (SLM) are used to achieve 3D light field projection. The proposed method can improve the throughput of the fabrication process compared to serial spot by spot or layer by layer fabrication methods since the virtual 3D structures can be reconstructed from a single projection. Unlike holographic lithography, we do not require coherent light sources since light field imaging does not require stable interference patterns for operation. Hence, incoherent light sources can be used in 3D light field lithography without forming unwilling speckles. Section 2 will discuss the theory of the 3D light field or plenoptic imaging, followed by a discussion of our in-house 3D light field projection system in section 3. Section 4 will briefly discuss two-photon 3D light field lithography results. Section 5 will summarize the findings in this thesis along with future works.

2. 3D LIGHT FIELD IMAGING

2.1. Overview

The 3D light field imaging, also known as integral photography (IP), was proposed by Lipmann to enable us to view a 3D object at different depths. Before this concept came up, 3D depth perception was more based on physical mechanisms, which involved accommodating the disparity between different retinal images at different depths of the same object and convergence of the visual axes. While observing distant objects, the disparity is less, and the accommodation is relaxed with parallel visual axes. On the contrary, while observing closes objects, a stronger accommodation is implemented on the eyes with a remarkable convergence of the visual axes to achieve a significant disparity. Based on this information and physical clues provided by optic nerves, the brain can perceive and estimate the depth of the 3D object.

Volumetric displays, which can display 3D volumetric images in true space, became more common along with the concept of holography. But holography could not be applied for wide 3D displays due to the requirement of a greater number of small-sized pixels in the photographic film and the need for refreshable and real-time updateable materials. The 3D light field imaging concept introduced by Lipmann in 1908 then became very useful. He proposed using a microlens array (MLA) in front of a photographic film to capture a collection of elemental 2D images, each with a unique perspective of the 3D scene. The primitive system of Lipmann concept that was only used to display the 3D scene using these elemental images suffered few drawbacks. The elemental images tend to overlap for a wider 3D scene, and the microlens array could only be used to capture scenes closer to the camera. Coffey modified the system by using a field lens of a larger diameter to fit the 3D scene onto the MLA. This allows the usage of a conventional photographic camera as in the Lipmann system with minimum overlapping of elemental images. With the advancement in quality and speed of pixelated optoelectronic sensors and displays, integral photography slowly transformed into Integral Imaging (InIm) by a few other authors by proposing different capturing and transmitting techniques of the integral images. Soon after, the first plenoptic camera was introduced by Adelson and Bergen in 1991 as an updated version of Coffey's camera. They reported the plenoptic formalism, which describes any luminous ray in space as a function of angle and position. The InIm technology has many different pathbreaking applications and has been an efficient solution to many technological problems with a substantial interest in entertainment, medicine, security, defense, transportation, and manufacturing. Some biomedical applications involve endoscopy, static or dynamic deep tissue inspection, otoscopy, and ophthalmology. Other uses include giga pixel photography, a 3D inspection of road surfaces, 3D polariscopy. Perhaps the most important application of all is 3D integral or light-field microscopy, which allows microscopists to observe a sample reconstructed in 3D space from different perspectives in real-time.

2.2. Fundamentals of 3D integral imaging

Any point in a 3D object emits a cone of rays that contain angular information for each ray. Any optical instrument that can capture and integrate this angular information will give us perspective information on the 3D scene as in the human eye. Light field cameras, also known as plenoptic cameras, are a special type of camera that can capture both the intensity and spatial-angular information of light field emanating from a 3D scene when conventional cameras can record only intensity information. A light field camera looks like a traditional camera but has a microlens array in front of the image sensor to sense color, intensity, and directional information of the 3D scene. All light field cameras work on multiscopic 3D imaging, also known as integral imaging, where a 2D array of microlenses can capture and reproduce the entire 3D scene without the aid of a large viewing lens. A large 3D scene can be divided into micro images or elemental images captured by individual microlens as seen from its viewpoint during capture mode. During the reproduction or refocusing mode, the image sensor coupled to the microlens array allows the viewer only to see the area of the associated micro images that needs to be reproduced [46]. While the microlens array preserves the spatial and angular information of different regions in a 2D object plane, the intensity information is obtained by integrating the pixels on the image sensor, as shown in *Figure 9*.

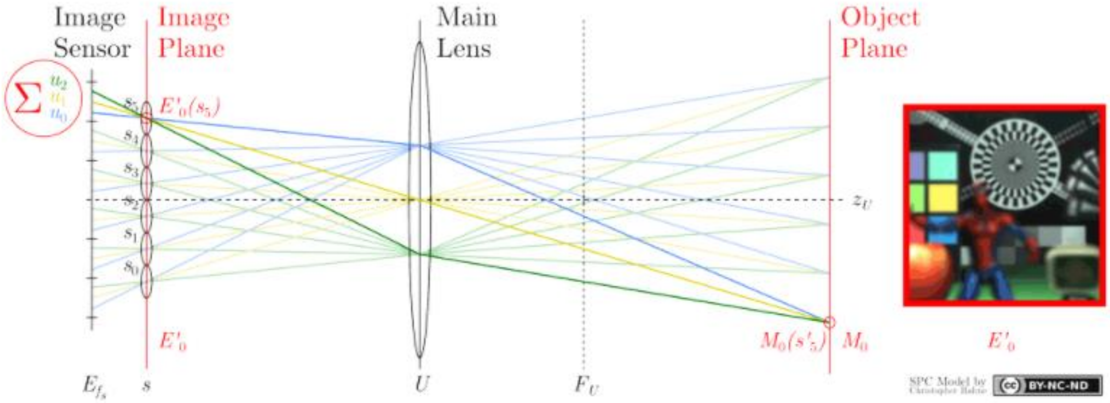

Figure 9: Illustration of refocusing in 3D light field cameras. Each point on the object plane is associated with one or more microlenses for spatial information, and the intensity information is obtained by integrating the pixels formed by the point on the image. Reprinted from [47]

This technique is a complete visual reproduction of depth cues, a perspective that changes with the distance and position of the observer. When microlenses become smaller, more micro images can be formed to sufficiently improve the quality of refocusing and necessary accommodation in the eye focus to view objects at different distances. Unlike real volumetric displays, the images perceived through these microlenses are virtual and have one subjective location in space, allowing a scene with infinite 3D depth to be displayed without needing other focusing lenses [48]. Integral imaging captures a normal scene and enables the viewer to focus on different points, thus giving a 3D perspective of the scene, as shown in *Figure 10*.

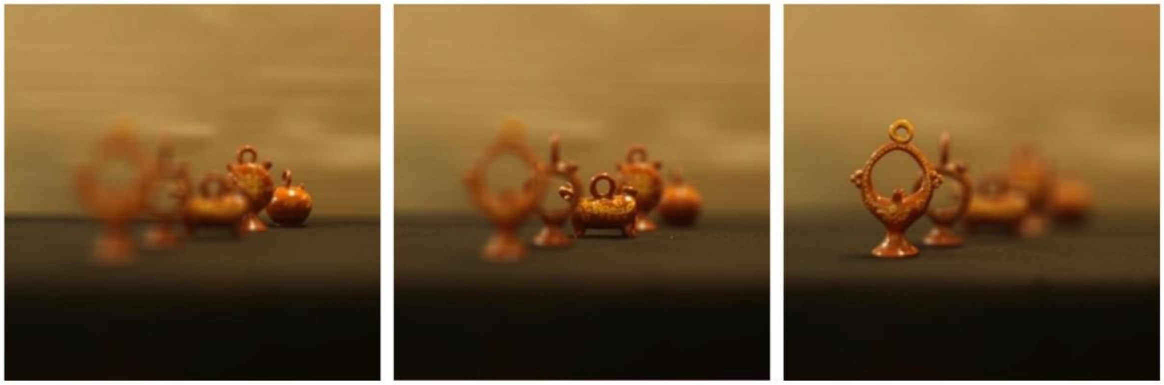

Figure 10: Images obtained after refocusing at three different z depth values. Reprinted from [46]

Light field cameras are divided into two categories. The first type is the unfocused light field camera proposed by Adelson and Wang in 1992 [49]. The other type is the focused light field (FLF) camera proposed by Lumsdaine [50]. Although the two types have a similar setup, the cameras differ in the distance between MLA and sensor array. The detector array is placed at the back focal plane of the MLA in the unfocused light field camera. On the other hand, the FLF camera forms an intermediate image after the MLA in a Galilean configuration or before the MLA in a Keplerian configuration. The detector array is placed before and after the MLA back focal plane in Galilean and Keplerian configuration to obtain a sharp image. The configurations are illustrated in *Figure 11*

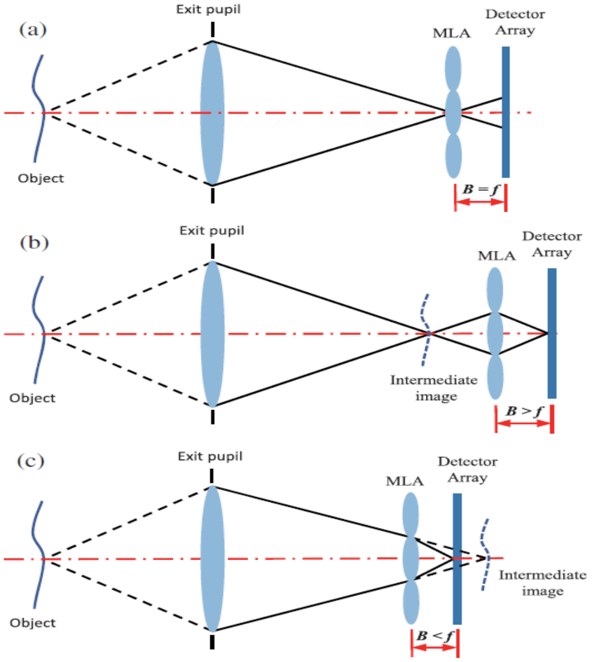

Figure 11: Schematic of light field cameras. (a) Unfocused light field camera (b) Keplerian focused light field camera c) Galilean light field camera. f is the focal length of microlens array MLA. B is the distance between MLA and detector array. Reprinted from [51].

2.3. Depth reconstruction and resolution

In the case of an unfocused light field camera, the distance between the exit pupil of the imaging lens and MLA is much larger than the focal length of the MLA. This enables the MLA to image the exit pupil onto the sensor array completely. The cartesian coordinates at the exit pupil and the MLA are denoted by (u, v) and (x, y) respectively. A 4D light field data cube can be formed by extracting corresponding pixel intensities from the raw image capture. As shown in *Figure 12*, a 2D (x, u) slice known as epipolar plane image can be formed from this data. The EPI contains line structures associated with rays emitted by points S_1, S_2, and S_3. These line structures are monotonic functions of the depth of these object points. In a ULF camera, the depth of an object can be rendered by measuring the slope of its line structure in EPI. Reconstructing images at every depth gives a focal stack, and an extended depth of field image can be formed by combining these reconstructed images with a fusion algorithm.

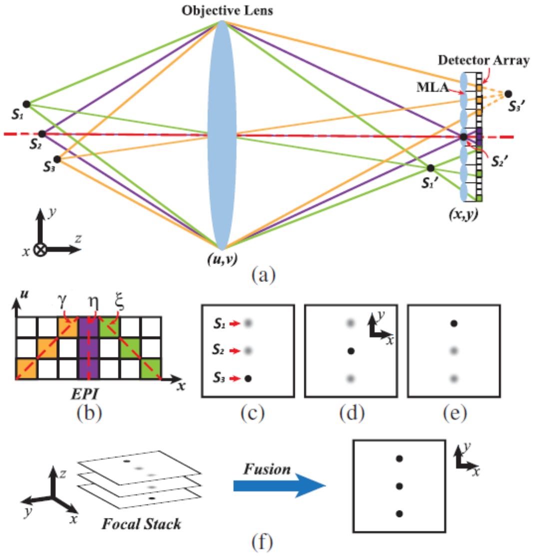

Figure 12: Image acquisition in ULF camera. a) Image formation in ULF camera. b) Sample epipolar plane image EPI having three-line structures with slopes γ,η, and ξ. c-e) Refocusing through light field integration along these line trajectories. f) Extended depth of field image reconstruction. Reprinted from [51].

In the case of a focused light field camera, the distance between MLA and objective lens is not so large compared to ULF cameras. As a result, an intermediate image from the objective lens is formed behind or in front of the MLA. The MLA then relays this intermediate image onto the detector array. As shown in *Figure 13*, subimages are formed behind each microlens, and the depth information of the object point can be found by measuring the disparities between these subimages. Essentially in each subimage, the purple pixel denotes the light rays converging to the same virtual point S’. Grouping all such pixels and mapping their values to a single-pixel yield the reconstructed image. This is then repeated for each pixel to reconstruct the entire 3D scene.

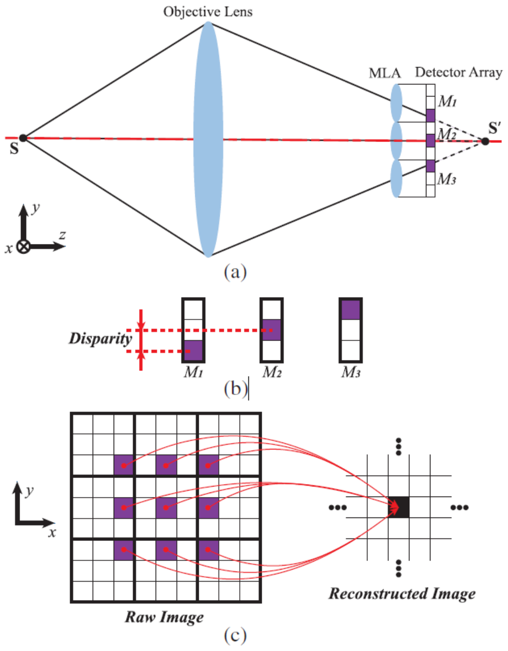

Figure 13: Image acquisition in FLF camera (Keplerian) a) Image formation b) Disparity calculations in sub images *M_1*, *M_2*, and *M_3*. c) Image reconstruction schematic in an FLF camera. Reprinted from [51]

2.4. Resolution study

2.4.1. Depth of field and lateral resolution

As shown in Figure 14, the condition $B = f$ corresponds to unfocused light field camera and $B < f$ and $B > f$ corresponds to focused light field camera. t denotes the diameter of the blurred image point on the detector array. A light field camera acquires not only the image of an object but also its depth map. For calculating the depth range, a criterion is setup for maximum acceptable blur diameter. Depth of field (DOF) of a light field camera is defined as the range in intermediate image space where the blur diameter in the reconstructed image is not more than the acceptable blur diameter.

Due to the diffraction effects of light, the points O_1 and O_2 are not ideal points, but spots with radius $r_s = \frac{0.61\lambda}{NA}$ where λ is the wavelength of light and NA is the numerical aperture of the microlens. If r_s is greater than pixel size p of the sensor, then the lateral resolution is limited by r_s. The minimum resolvable spot size s_e is defined as

$$s_e = \max{(r_s, p)} \tag{1}$$

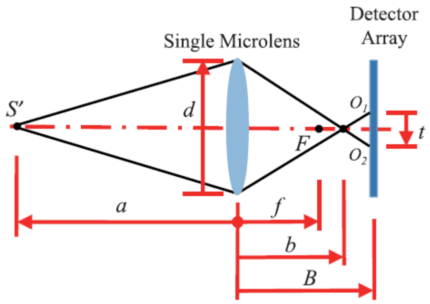

Figure 14: Intermediate image point S' imaged by a single microlens. Reprinted from [51]

In the case of unfocused light field cameras, the DOF is the depth range within which the blur diameter is not greater than the diameter of single microlens. As shown in Figure 15 for the intermediate image point S' in front of MLA $a < 0$, the disparity Δ of two image spots in the sub images is

$$\Delta = -\frac{df}{a}$$

(2)

As per definition, if S' is in the DOF, then its image occupies only a single pixel in the reconstructed sub-aperture image. For this $\Delta > \ s_e$, which gives $a > \frac{-df}{s_e}$. Similarly, when $a > 0,\ a < \frac{df}{s_e}$. Hence, the depth of field of an unfocused light field camera is

$$DOF_{ULF} = \left[\frac{-df}{s_e}, \frac{df}{s_e}\right]$$

(3)

The lateral resolution of a light field camera is determined by the effective pixel size p_e as

$$LR = \frac{1}{2p_e}$$

For a ULF camera, this effective pixel size equals the diameter of the microlens when the intermediate image is in the DOF.

$$LR_{ULF} = \frac{1}{2d} \tag{4}$$

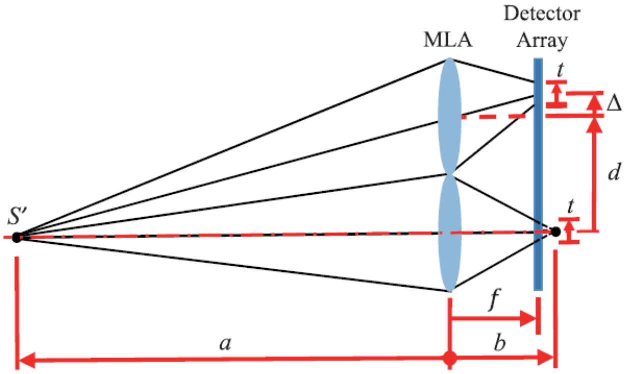

Figure 15: Calculation of DOF in a ULF camera. t is the image spot size. d is the distance between two imaging microlenses. Δ is the disparity between the image spots within sub images. a and b are the object and image distances of the microlenses, respectively. Reprinted from [51].

In the case of a focused light field camera, *Figure 16* shows an intermediate image refocused by a single microlens in a Galilean configuration. Using trigonometric equations, the blur diameter in the subimage t_2 is

$$t_2 = \frac{d(B-b)}{b}$$

(5)

Using the thin lens equation, $\frac{1}{b} = \frac{1}{a} + \frac{1}{f}$, the blur diameter is

$$t_2 = d\left[B\left(\frac{1}{a} + \frac{1}{f}\right) - 1\right]$$

(6)

Since the maximum acceptable blur diameter is defined at the plane where S' is located, the blur spot at the detector array is projected to plane of S' with an MLA magnification of $m = {}^{B}/_{a}$

The blur diameter at the plane of S' is

$$BD = \frac{\max\,(t_2, s_e)}{|m|}$$

(7)

The acceptable blur diameter for FLF camera is also set to the diameter of single microlens d

$$DOF_{FLF} = \left\{a: \left|\frac{a}{B}\right| max\left\{\left|d\left[B\left(\frac{1}{a} + \frac{1}{f}\right) - 1\right]\right|, s_e\right\} < d\right\}$$

(8)

Similar to UFL camera, the lateral resolution is determined by the effective pixel size p_e and it equals the blur diameter BD. Hence,

$$LR_{FLF} = \frac{1}{2BD} = \left|\frac{B}{2a}\right| \frac{1}{max\left\{\left|d\left[B\left(\frac{1}{a}+\frac{1}{f}\right)-1\right]\right|, s_e\right\}}$$

(9)

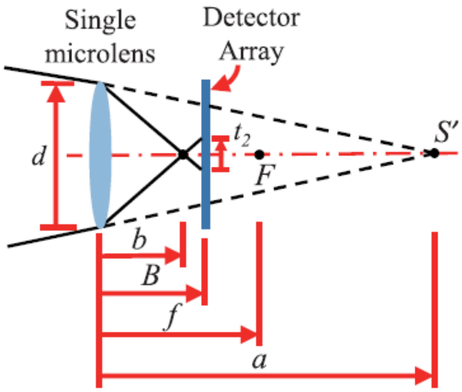

Figure 16: Calculation of DOF of an FLF camera.t_2 is the blur diameter in the sub image. Reprinted from [51].

2.4.2. Depth resolution

The depth resolution of a light field camera is defined as the smallest detectable depth change. As shown in *Figure 17*, any intermediate point S’ can be reimaged by the microlens array onto the image sensor. The microlens closest to the point is denoted by L_0 and all the microlens above and below this are labeled as L_{-1}, L_1 etc. respectively. u_i is the distance between the intersection of a chief ray of a microlens L_i and the center of that microlens. For the microlens L_i to image the point S’,

$$u_i = \frac{B(d_0 + id)}{a} \in \left[-\frac{d}{2}, \frac{d}{2}\right]$$

(10)

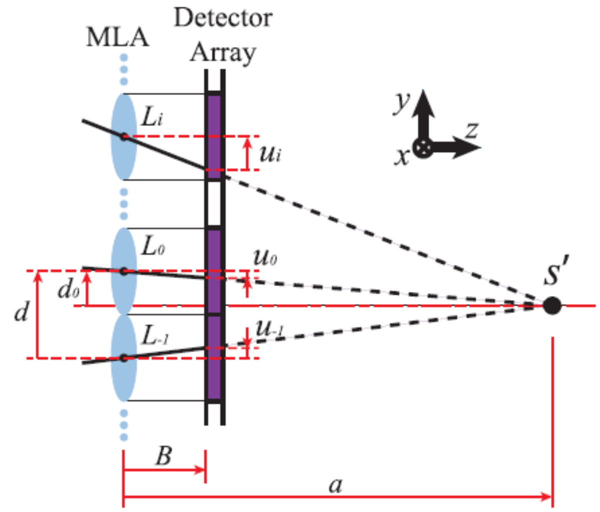

Figure 17: Intermediate image point S’ reimaged by microlenses in a light field camera. Reprinted from [51]

In the unfocused light field camera, the depth of point S’ is measured by measuring the slopes of lines in EPI. For the EPI shown in Figure 18, the angle α can be calculated as

$$\tan\alpha = \frac{p}{u_i - u_{i-1}}, |u_i| < \frac{d}{2}$$

(11)

where p is the pixel size in the image sensor. Combining equations (10) and (11),

$$a = \frac{Bd}{p}\tan\alpha$$

(12)

For the smallest increment of $\delta\alpha$ that can be detected, the depth resolution of the ULF camera can be defined as

$$DR_{ULF} = |a(\alpha + \delta\alpha) - a(\alpha)| = \left|\frac{Bd}{p} tan(\alpha + \delta\alpha) - tan(\alpha)\right|$$

(13)

Combining equations (12) and (13), the final expression for depth resolution for an unfocused light field camera is

$$DR_{ULF} = \left|\frac{(a^2p^2 + B^2d^2)\tan(\delta\alpha)}{p[Bd - ap\tan(\delta\alpha)]}\right|$$

(14)

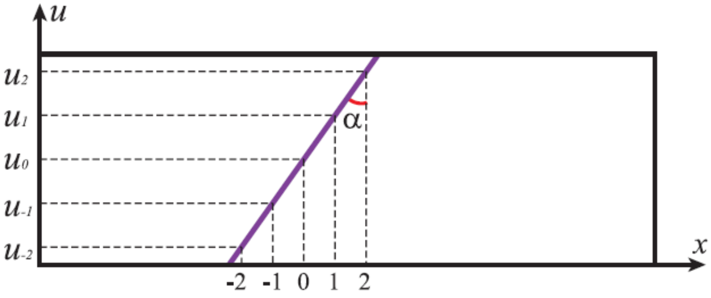

Figure 18: Epipolar plane image of a ULF camera. Reprinted from [51]

In the case of focused light field cameras, the depth of point S' is measured by measuring the disparity between sub images. As shown in *Figure 19* for an FLF camera, the range of microlenses between L_{max} and L_{min} found by equation has two arbitrary microlenses in the center L_r and L_s. The respective sub images behind these microlenses are M_{min}, M_{max}, M_r, and M_s. In an FLD camera the line connecting the central points of subimages are known as baselines, and the depth is found by measuring disparities between these baselines. As shown in the figure, the disparity can be calculated as

$$\Delta u = |u_r - u_s| = \frac{Bd}{a}(r - s) = \frac{Bh}{a}$$

(15)

which on rearranging gives

$$a = \frac{Bh}{\Delta u}$$

For the smallest detectable increment f disparity that can be resolved completely by FLF camera, the depth resolution is given by,

$$DR_{FLF} = |a(\Delta u + \delta\Delta u) - a(\Delta u)| = \left|\frac{a^2\delta\Delta u}{Bh + a\,\delta\Delta u}\right|$$

(16)

DR_{FLF} decreases with an increase in h, which improves the resolution of the FLF camera. But for larger values of h, the incident angle of light rays is also larger. This results in increased aberrations in the corresponding sub images, which degrades the quality of the images. Hence to balance this, only adjacent microlenses are used to calculate disparities.

$$DR_{FLF} = \left|\frac{a^2\delta\Delta u}{Bd + a\,\delta\Delta u}\right|$$

(17)

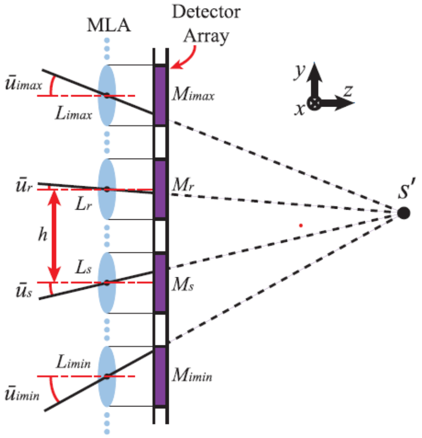

Figure 19: Intermediate image point S' imaged by microlenses in FLF camera. Larger incident angles for edge microlenses chief rays causing aberrations. Δu is the disparity in sub images. Reprinted from [51]

By simulating and comparing the depth resolution between a ULF and FLF camera based on equations (3) and (8), it was found that the ULF camera has a greater depth resolution than an FLF camera. However, the lateral resolution of an FLF camera in this depth range, as represented by equation (9), is more acceptable compared to a ULF camera represented by equation (4). Similarly, the depth resolution of an FLF camera deteriorates with an increase in depth for equation (17), whereas the ULF camera has a constant depth resolution represented by equation (14). Hence ULF camera outperforms its focused counterpart in depth resolution, whereas the FLF camera has an advantage in lateral resolution and reconstruction accuracy [51]. The following chapter will discuss how to implement the physics used in light field cameras to create our in-house DMD-based 3D light field projection system. We will also perform a resolution study to determine which configuration of our light field projection can provide good lateral and depth resolution. Later in this thesis, we will discuss how our 3D light field projection system can achieve single-photon and two-photon lithography.

3. 3D LIGHT FIELD PROJECTION

A microlens array-based 3D light field projection system inspired by light field cameras was proposed and reported by our research group [52]. As discussed in the previous chapter, light field cameras have the unique capability to achieve 3D imaging by inserting an MLA into a traditional camera. By inverting the operation direction of a light field camera, we can achieve 3D light field projection to create 3D virtual objects in free space.

3.1. Physical basis

In the proposed method, a spatial light modulator (SLM), the equivalent of a detector array in the inverted setup, is kept at the front focal plane of the microlens array, similar to the unfocused light field camera arrangement. A digital micromirror device (DMD) type SLM is used to send light rays. DMD-based 3D light field projection is not exactly the inverted process of integral imaging since DMD can only control each pixel's on and off states individually but not the intensities and directions. A nearly parallel beam of light is delivered from the SLM to the MLA, which causes all the incident light to pass through the focal point of each microlens. The angle of light coming from each pixel cannot be controlled individually with the DMD. Hence the intensity of the light field drops with an increase in z depth due to divergence after the focal plane. This is compensated by adding more pixels to deeper z locations.

To construct a 3D surface, the surface is first discretized into individual voxels or point clouds in 3D space. For each of those voxels, we determine the active microlenses. Active microlenses are those microlenses that can form that voxel point within its limited numerical aperture. Then we choose the corresponding pixels within these active microlenses to be turned. The resultant pixel map is then loaded to the SLM to reconstruct a virtual 3D object at designed locations in 3D space.

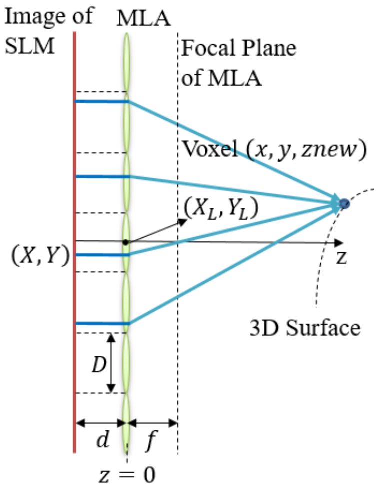

Figure 20: Microlens array-based 3D light field projection system. Reprinted from [52]

As shown in *Figure 20*, for any intended voxel point (x, y, z) in 3D space, the corresponding pixel (X, Y) that need to be turned on for its projection is determined by geometrical optics. An active microlens with center (X_L, Y_L) that projects the voxel (x, y, z) should satisfy the condition

$$\sqrt{(X_L - x)^2 + (Y_L - y)^2} \leq \frac{D(z - f)}{2f} \tag{18}$$

The corresponding pixel (X, Y) within each active microlens can be calculated using the equation

$$X = X_L - \frac{f}{z-f}(x - X_L)\ ;\ Y = Y_L - \frac{f}{z-f}(y - Y_L)$$

(19)

Only a specific area under each microlens is used to improve the quality of the 3D projection, as shown in *Figure 21*. The ray behavior at microlens boundaries is unknown, so the usage of microlens boundaries is avoided, which is indicated by parameter α. Also, to reduce the focused voxel size, the pixels at the center are avoided, which is characterized by parameter β. Any active microlens with center (X_L, Y_L) that projects the voxel (x, y, z) should satisfy the new condition

$$\frac{\beta D(z-f)}{2f} \le \sqrt{(X_L - x)^2 + (Y_L - y)^2} \le \frac{\alpha D(z-f)}{2f}$$

(20)

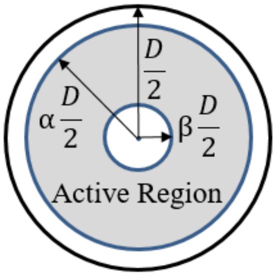

Figure 21: Active pixels region within each microlens. Reprinted from [52]

To verify the capability of our system to project 3D structures, two concentric rings were designed at different depths, as shown in *Figure 22b*. Two concentric rings with different diameters were designed to be projected at $6f$ and $8f$ locations. The corresponding pixel value map of our designed structure was calculated using the above-mentioned geometric correlations. The pixel value map, which is shown in *Figure 22a*, is uploaded to the SLM.

The 3D projections were imaged plane by plane using a secondary telecentric lens pair coupled with a CCD camera. When the inner ring at 6f plane is focused, the outer ring at 8f is blurred and vice versa, as shown in the figure. The CCD images verify that real 3D objects can be reconstructed with this system.

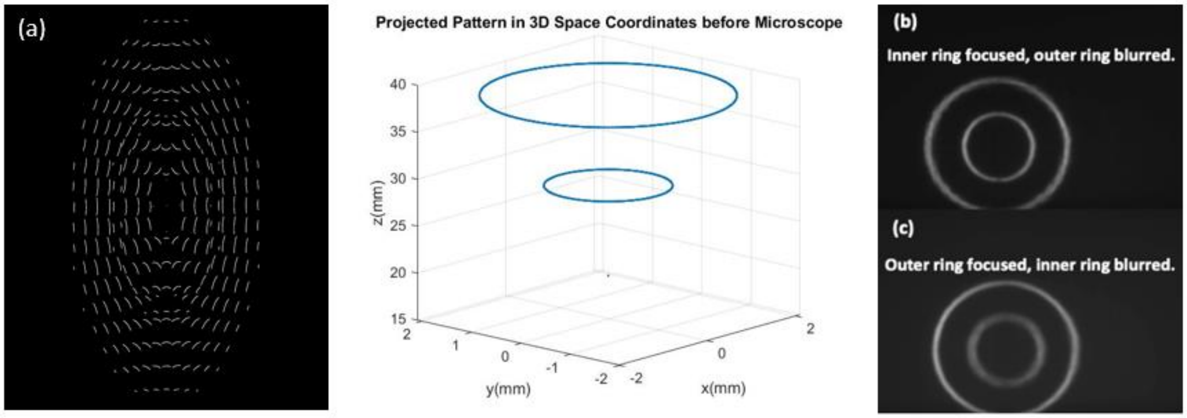

Figure 22: a) SLM pixel value map for projecting two concentric rings at different z locations b) Inner 6f ring sharp and outer 8f ring blurred. c) Inner 6f ring blurred and outer 8f ring sharp.

3.2. Single-photon 3D light field lithography

The experimental setup of the 3D light field projection system is shown in *Figure 23* [53]. A 405 nm UV LED source delivers light to digital micromirror device based SLM (DLP LightCrafter 4500 Texas Instruments). The desired 3D structure to be formed is discretized into individual voxels, and the pixel map for the entire object is loaded to the SLM through a USB cable. The light from these selected pixels is delivered to the designed voxel locations through an MLA (Edmund Optics 86-745) with $f = 4.8$ mm and pitch $D = 300$ µm. A telecentric lens pair is an optical relay that provides the pixel map directly before the MLA with 1:1 magnification. This enables us to easily control the distance between pixel map and MLA for trying different configurations. A spatial filter is used in the optical relay to limit the divergence angle of the parallel beam towards the MLA.

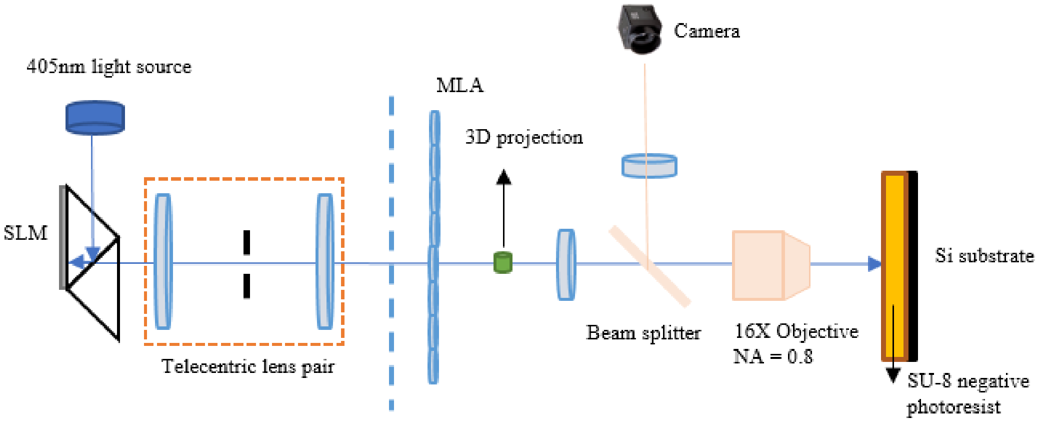

Figure 23: Experimental setup of our 3D light field lithography system. Reprinted from [53]

The 3D projection is further delivered to a telecentric lens pair constructed with a 200 mm tube lens and infinity-corrected 16X objective lens (Nikon 16X DFI LWD Plan Fluorite NA =

0.8). Additionally, a beam splitter is inserted in the second stage telecentric lens pair to real-time inspect the projected 3D patterns with a CCD camera. The second stage telecentric lens paired with a CCD camera is essential for calibration of the relative positions of the SLM and MLA. The lateral size of the 3D projection is compressed by 16 times, and the longitudinal size is compressed by 256 times using the objective lens. The compressed microscale 3D projection is then delivered to a SU-8 photoresist spin-coated on a Si wafer to achieve photolithography.

Although our MLA-based 3D light field projection system has a high potential to project and pattern 3D objects in the photopolymer, the intensity at deeper z locations is significantly reduced due to the focusing and diverging effect associated with the DMD- MLA setup. Since the spectral absorption range of SU-8 lies in the UV region, significant light absorption takes place within SU-8 along the z-direction. This should be compensated by having more rays for deeper voxel locations during lithography. Additionally, the single-photon absorption in the photopolymer causes unwilling curing of the photopolymer along the optical path of the light rays, as shown in *Figure 24a*. This results in a size mismatch between the fabricated patterns and the design.

It is expected that this unwilling curing along the optical path can be prevented by replacing the UV LED light source with a femtosecond laser source. The high intensity of femtosecond light can induce two-photon absorption and polymerization within SU-8, resulting in curing only at the designed voxel locations, as shown in *Figure 24b*. By using 520 nm fs light, the absorption within SU-8 is also expected to be prevented. The two-photon polymerization phenomena will be discussed in the next section.

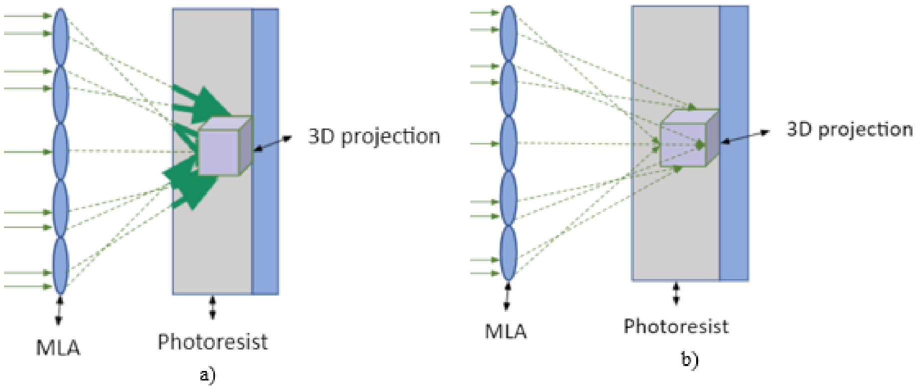

Figure 24: a) Unwanted curing in the photoresist along the optical path due to single-photon absorption (solid lines) b) Curing only at the designed voxel locations and not along the optical path (dotted lines) in two/multi photon absorption

3.3. Two-photon polymerization

Two-photon or multiphoton polymerization proceeds by absorbing two photons or multi photons simultaneously. Liquid materials or resins can be converted to solid either by cross photo linking or photopolymerization, where the former involves crosslinking between macromolecule chains. In contrast, photopolymerization involves the creation of photopolymers through light-induced chain reactions. These chain reactions are proceeded by crosslinking between monomer molecules containing more than one reactive group. However, these monomers and oligomers do not have sufficient initiating species for chain reactions upon enough light exposure. So low molecular weight molecules called photo initiators are added to initiate polymerization. In addition to a photo initiator, photosensitizers are also added to increase the light absorbance to transfer the excitation to the photo initiators directly. Depending on whether cations or radicals initiate the polymerization, the photopolymerization can be categorized into a) Cationic polymerization (Ring-opening reactions in epoxides) b) Radical polymerization (acrylates reaction). [54]

In a typical one-photon absorption case, like UV lithography, the photo initiator is excited by a single photon by a higher singlet state with a lower half-life which decays immediately to a forbidden triplet state having a much longer half-life which allows emissions immediately after excitation. A good photo initiator design with longer triplet lifetimes will form sufficient radicals for initiating photopolymerization. Unlike UV lithography, two-photon polymerization (2PP) involves a focused, intense laser beam of the order terawatts per $cm^{2,}$ associated with two-photon or multiphoton absorption simultaneously with a photo initiator, or a possible dielectric breakdown or avalanche ionization which proceeds without a photo initiator. With such high fluence of the irradiating tightly focused laser beam is sufficiently high, the probability of an electron absorbing two photons simultaneously becomes very high. The valence electrons in a photoinitiator are excited from the ground state (S_0) to the first excited (S_1) singlet state, as shown in *Figure 25*, by absorbing two photons simultaneously. The rest of the process is like single-photon polymerization. The excited electrons relax by transitioning into an intermediate (T1) triplet state that emits free radicals required for polymerization by undergoing bond cleavages. Radicals formed by these photoinitiators must have high reactivity with the monomers to produce monomer radical, extending on its own by reacting with other monomer molecules until polymerization terminates.

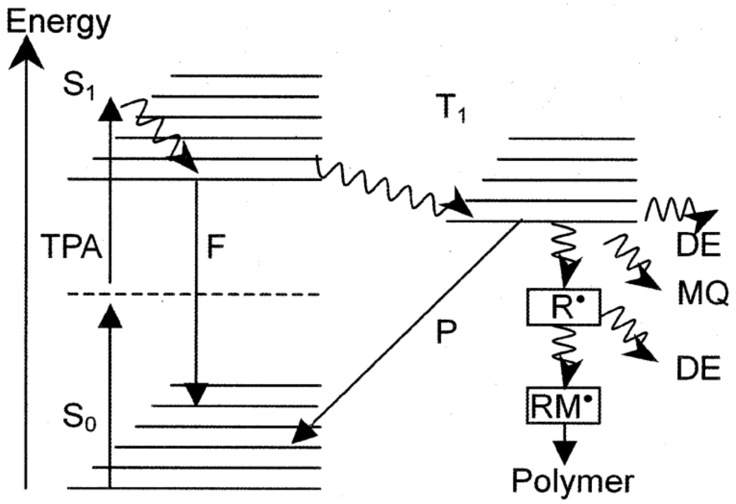

Figure 25: Energy diagram for two-photon absorption (TPA). S_0 is the ground state of valence electrons in the photoinitiator, and S_1 is the first excited singlet state. T_1 is the intermediate triplet state. Initiator in the triplet state undergoes bond cleavage and forms radicals R, which reacts with monomer to polymerize (RM). The excited singlet state and triplet state can be relaxed by radiative processes like fluorescence emission (F) and phosphorescence emission (P). The triplet state can be deactivated by monomer quenching (MQ), and radicals can also be deactivated by radical quenching (RQ). Reprinted from [40]

In ultraviolet light-based stereolithography (SLA), light as a tool interacts only with the photopolymer surface. This is the reason why UV-based additive manufacturing is termed as layer by layer process. 2PP breaks free from this paradigm due to the absence of this tool path limitation. 2PP utilizes the two-photon absorption of slightly higher wavelength light to excite the same energy transition as ultraviolet (UV) photons. Since the 2PP photopolymer is transparent to this fundamental wavelength, the 2PP technique can process material at any point within the photopolymer. This difference between single-photon and two-photon absorption for fluorescence microscopy is shown in Figure 26. Three-dimensional micromanufacturing by femtosecond two-photon polymerization is an appealing technique for producing microscale devices due to its flexibility in producing structures with a wide range of geometries as well as its compatibility with materials suitable for biomedical applications.

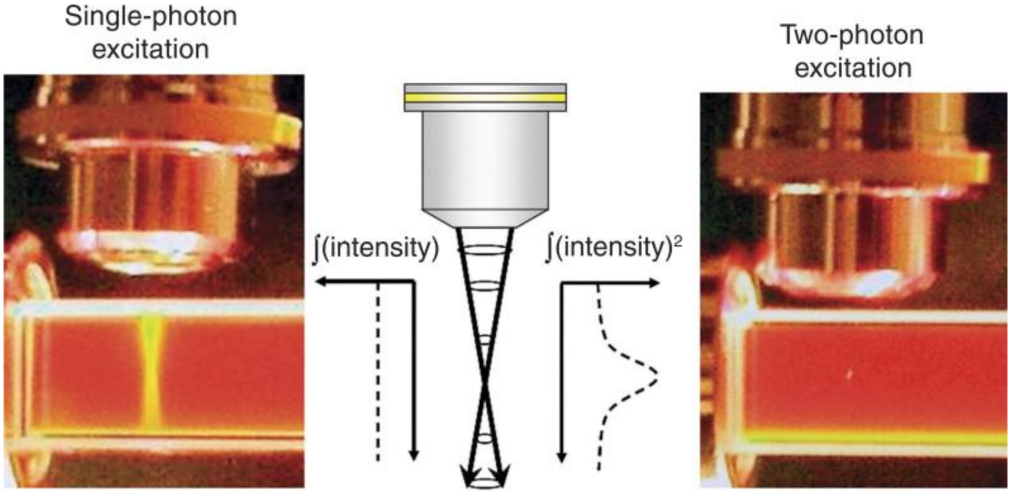

Figure 26: Fluorescence in rhodamine B solution by single-photon excitation from the UV lamp and two-photon excitation from NIR Ti:Sapphire femtosecond laser. Reprinted from [55]

3.4. Study of system resolution

It is crucial to study the resolution of our DMD-based 3D light field lithography system to determine the ideal configuration distance between the SLM image plane and the MLA plane. For simplicity, a voxel on the optical axis with $x = 0, y = 0$ is considered.

The lateral resolution of this system is defined as the smallest lateral voxel size that can be projected by our system. As shown in *Figure 27*, the lateral resolution is limited by two parameters: 1) finite DMD pixel size, 2) finite size of the aperture stop or spatial filter in the first telecentric lens pair. Ideally, pixels are to be infinitesimally small or point-sized to form a point voxel in 3D space as indicated by the blue-designed ray in the figure. However, due to the finite size s of the SLM pixel, the lateral voxel size increases to Δx as shown in *Figure 27a*. From simple geometric correlations, it can be found that Δx is a function of z depth where the voxel is projected and the pixel size s.

$$\Delta x = \frac{s(z - f)}{f} \tag{21}$$

Another factor that limits the lateral resolution of the system is the finite size of the spatial filter. The aperture stop is used in the first telecentric lens pair to limit the divergence angle and only have parallel rays. But due to the finite size of our aperture stop, the light can have a small divergence angle θ which can also expand the voxel size in the lateral direction to δx as shown in *Figure 27b*. The divergence angle also depends on the light source. For an LED light, the divergence angle is usually larger than a more collimated fs laser source used in two-photon lithography. From geometric correlations, δx can be derived as a function of divergence angle θ and the z depth of the projected voxel

$$\delta x = 2d \tan\theta \left| 1 - \frac{z(d-f)}{fd} \right| \tag{22}$$

The digital lateral resolution of our system in projecting voxels for lithography can be calculated as the sum of two lateral voxel sizes mentioned above over the compression ratio M of the objective lens. The macro-sized 3D pattern after MLA is compressed by M times laterally by the objective lens before patterning on the photoresist.

$$DR_L = \frac{1}{M}(\Delta x + \delta x) \tag{23}$$

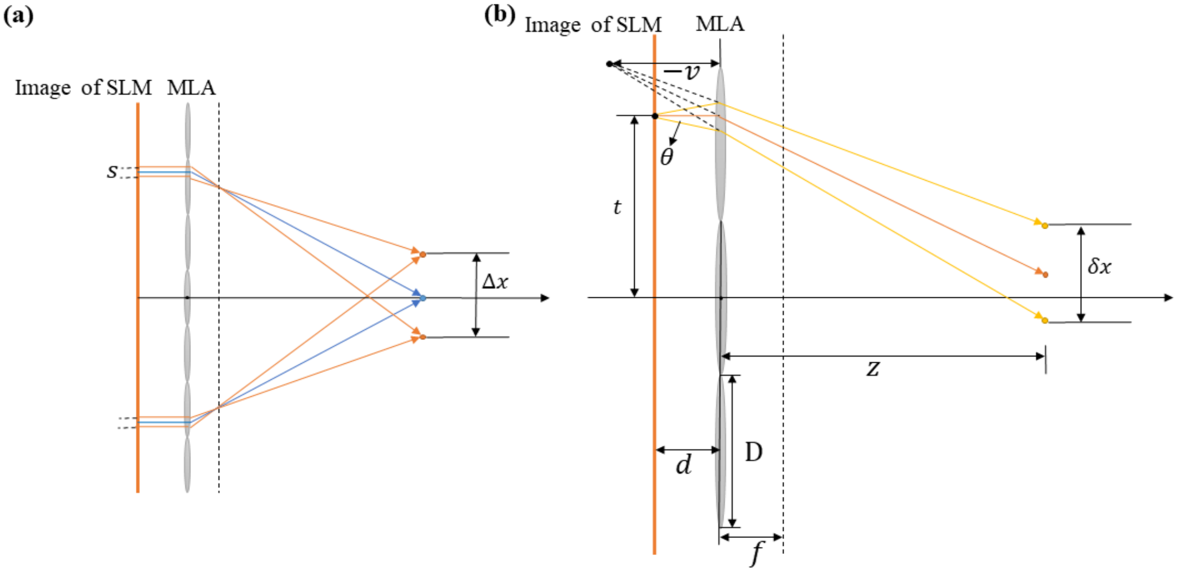

Figure 27:Illustration of lateral resolution of our 3D light field projection system resulting from (a) Finite-size of SLM pixel s. (b) Finite-size of aperture stop causing a small divergence angle θ. Reprinted from [52]

In the case of single photon lithography using UV LED light source, the divergence angle is assumed to be 0.6°, whereas, for the fs laser source, the divergence angle is assumed to be 0.2°. The SLM pixel size is approximately 10.8 μm, the focal length of MLA is 4800 μm, and the size of each microlens is 300 μm. Based on equation (23), the lateral resolution of our 3D light field projection as a function of z depth for different configurations is shown in *Figure 28*.

From the plot, different values of d have different lateral resolutions at different depths. $d = 1.1f$ is the best configuration as the lateral resolution remains almost constant at all z locations, especially in the regions of our projection, compared to other configurations. For different configurations, the lateral resolution decreases and increases, which means that light focuses at a particular depth and constantly diverges after that, expanding the voxel size as z depth increases.

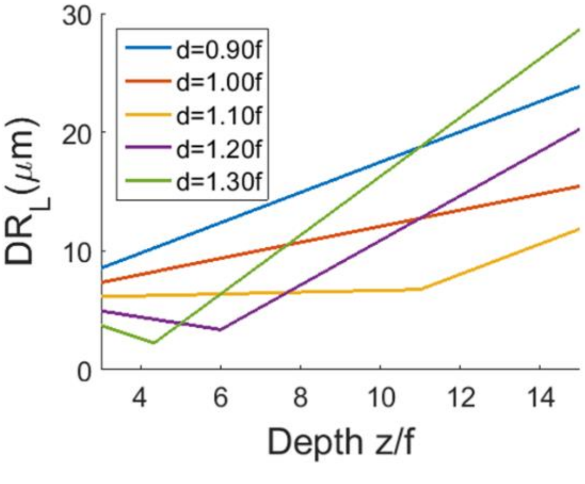

Figure 28:Digital lateral resolution plot as a function of z depth for our 3D light field projection system. Reprinted from [52].

The depth resolution can also be calculated similarly to lateral resolution. It is defined as the smallest voxel size in z-direction that can be projected by our system. The depth resolution is also limited by the finite size of SLM pixel s and the finite size of the aperture stop that causes light to have a small divergence of angle θ. As shown in *Figure 29c*, Δz can be derived using geometric equations

$$\Delta z = \frac{4iDfs(z-f)^2}{(2iDf)^2 - s^2(z-f)^2}$$

(24)

where i is the microlens center index depending on the microlens of interest.

$$i = \frac{\sqrt{{X_L}^2 + {Y_L}^2}}{D}$$

When $d < f$, the virtual image is formed on the left side of the MLA at a distance v. Using thin lens equation and geometric correlations δz_L and δz_R can be derived as

$$\delta z_L = z - v\frac{iD\frac{z}{z-f} - d\,tan\,\theta}{iD\frac{v}{z-f} - d\,tan\,\theta}$$

$$\delta z_R = v\frac{iD\frac{z}{z-f} + d\,tan\,\theta}{iD\frac{v}{z-f} + d\,tan\,\theta} - z$$

(25)

The cumulative depth resolution of the system is the sum of all these resolution distances over M^2. The macro-sized 3D pattern after MLA is compressed by M^2 times axially by the objective lens before patterning on the photoresist.

$$DR_z = \frac{1}{M^2}\left[\Delta z + \delta z_L(A) + \delta z_R(B)\right] \tag{26}$$

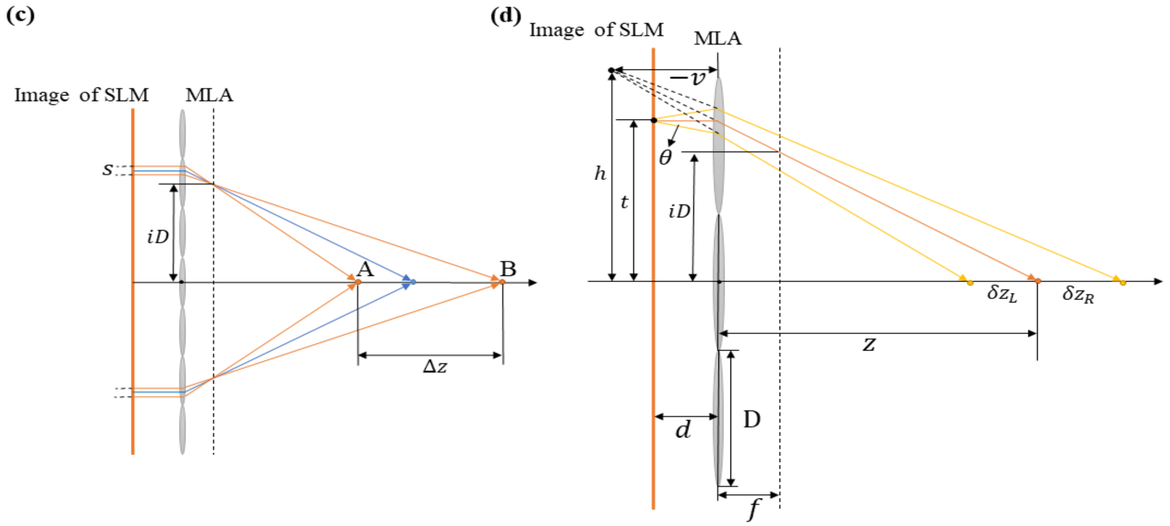

Figure 29: Illustration of depth resolution of our 3D light field projection system resulting from (c) Finite-size of SLM pixel s. (d) Finite-size of aperture stop causing a small divergence angle θ. Reprinted from [52].

Based on equation (26), *Figure 30* shows the depth resolution for our 3D light field projection as a function of z depth for different configurations. Like lateral resolution, different configuration values of d can have different depth resolution at different z depth values. As in lateral resolution, $d = 1.1f$ configuration also has a constant z depth resolution along z depth, especially in the regions of our 3D projections. The depth resolution plot is like an increasing step function because the z resolution of the voxel abruptly decreases whenever new microlens index values are considered in the expression. As shown in the equation, parameter i can potentially reduce the resolution of voxel size projected. Hence for the microlenses, the number of pixels in the center, controlled by the parameter β are minimized to improve the voxel resolution.

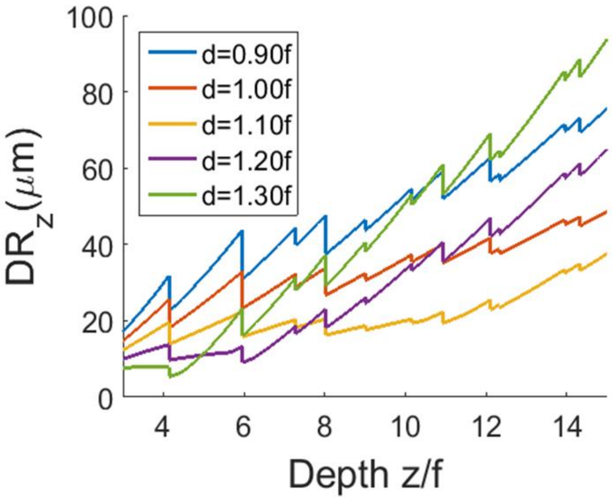

Figure 30: Digital depth resolution plot as a function of z depth for our 3D light field projection system. Reprinted from [52].

4. TWO PHOTON 3D LIGHT FIELD LITHOGRAPHY

Based on our group's successful demonstration of single-photon 3D light field lithography results in the past, this thesis focuses on extending the same methodology to a femtosecond laser source to achieve two-photon lithography. Compared to our previous single-photon 3D light field lithography system with UV LED light which caused unwilling curing along the path of light rays, femtosecond two-photon lithography can cure the photoresist only around the designed voxel locations. In addition to this, using a femtosecond light source and the associated two-photon polymerization in photoresists can provide better spatial resolution compared to UV LED single-photon polymerization. In section 4.1, we will discuss the experimental setup for our two-photon 3D light field lithography. Section 4.2 will discuss the preliminary test results for femtosecond two-photon 3D light field lithography based on voxel generation algorithms addressed in chapter 3. In section 4.3, we will further discuss how we can improve our voxel generation method to accommodate two photon absorption effects and improved photolithography results.

4.1. Experimental setup

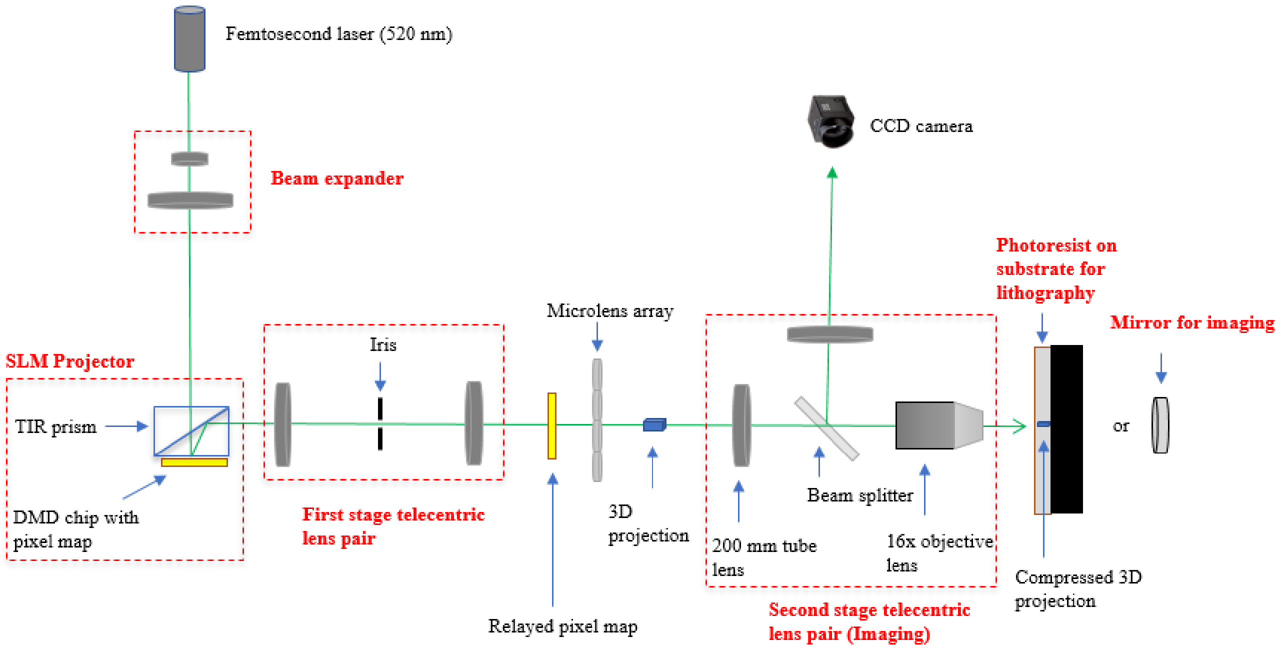

Figure 31: Schematic of a two-photon femtosecond 3D light field lithography system

A nearly uniform 520 nm femtosecond laser beam (~ 14 fs) chopped with beam expander and iris is adopted as the light source for the DMD type SLM. The beam provides a highly uniform profile around the center with sufficient intensity to cure the SU-8 photoresist. The uniformly expanded beam is then delivered to the spatial light modulator (SLM). Although the laser beam is highly collimated and uniform, an iris is added to the first stage of the telecentric lens pair to prevent higher-order diffraction patterns created by the laser when diffracted from the DMD gratings. The remaining components in the system are similar to the single-photon 3D light field lithography system discussed in section 3.2.

4.2. Preliminary two-photon lithography results

As a preliminary test for two-photon lithography, conical structures and tilted line with a wall structure were designed, discretized, and projected using the procedures followed in the single-photon LED lithography as discussed in chapter 3. For the designed cone structures, the base diameter was 250 μm and height was 112.5 μm. The voxels of the cone structure were spread from the 6f plane to the 12f plane of the coordinate system, as shown in *Figure 32b*. The corresponding pixel value map calculated from the old mapping procedure for single-photon lithography is shown in *Figure 32a*. The active MLA region was chosen to be as $\alpha = 0.9$ and $\beta = 0.1$. A 270 μm thick SU-8 photoresist after soft bake was used for exposure. The pixel vale map was then loaded to the SLM to expose the pattern on the photoresist for 2 mins. The resultant fabricated pattern after development is shown in *Figure 32d,e*. Unlike single-photon lithography, the height of the fabricated structure was in good correspondence to the design and was found to be 120 μm. This can be attributed to precise curing at each voxel point with two-photon absorption rather than curing along the optical path in the case of single photon absorption. However, the tapered structure of the cone was not achieved like in the case of single-photon lithography. The final fabricated cone structure does not have the tapered angle and has a cylindrical/ frustum shape-like feature. From the preliminary two-photon photolithography results for the cone, it can be seen that some undesired curing happens in the vicinity of our 3D pattern, which changes its final shape.

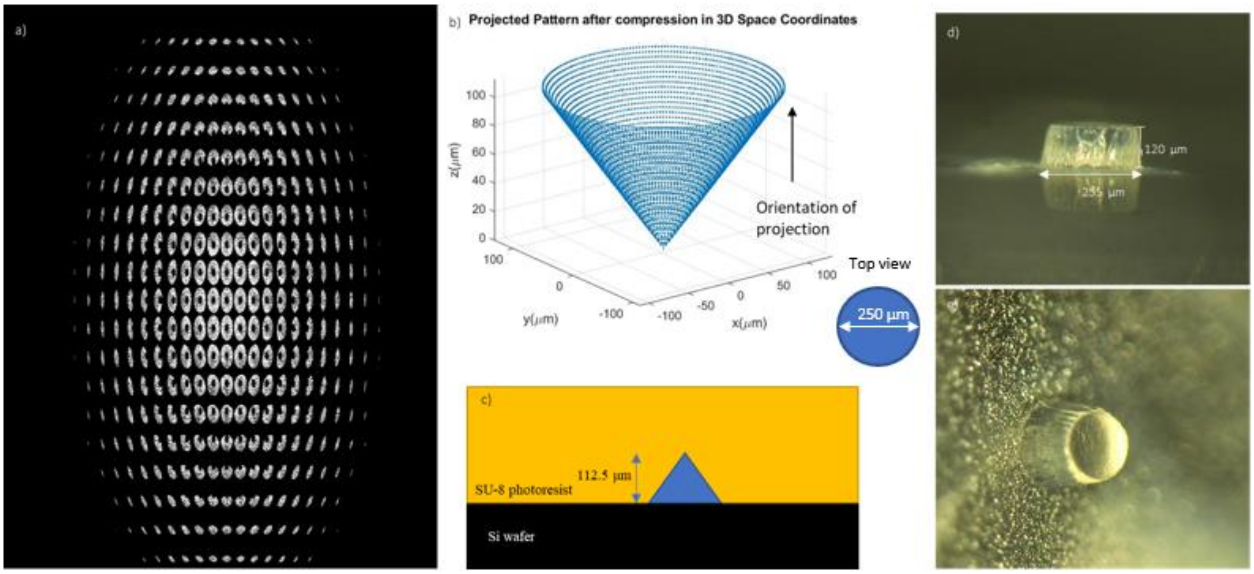

Figure 32: a) Pixel value map on the SLM to project the designed 3D structure. b) Voxel map of the designed cone structure after compression in real 3D coordinates. c) Illustration of the location of the projected 3D pattern inside the SU-8 photoresist. d)Photolithography result of cone structure (side view) e) Photolithography result of cone structure (top view)

The second test was carried out for long tilted line structures with one end attached to an over-exposed wall. The designed tilted lines were 360 μm long, 30 μm wide, and 112.5 μm (6f to 12f) in height, as shown in *Figure 33b*. The same active region of MLA $\alpha = 0.9$ and $\beta = 0.9$ was used and the corresponding pixel map is shown in *Figure 33a*. The pattern was exposed for 3 mins, and the fabrication result is shown in *Figure 33d,e*. The results revealed that the final shape of the tilted line was a straight plateau. This can be attributed to undesired curing around the tilted line, similar to what was observed in cone patterns. The height of the tilted line 130 μm was close to the design height, but regions above and below the tilted lines were also cured in the process. From the preliminary two-photon photolithography results for tilted lines, it can also be seen that unexpected voxels are formed and can alter the final shape of our pattern.

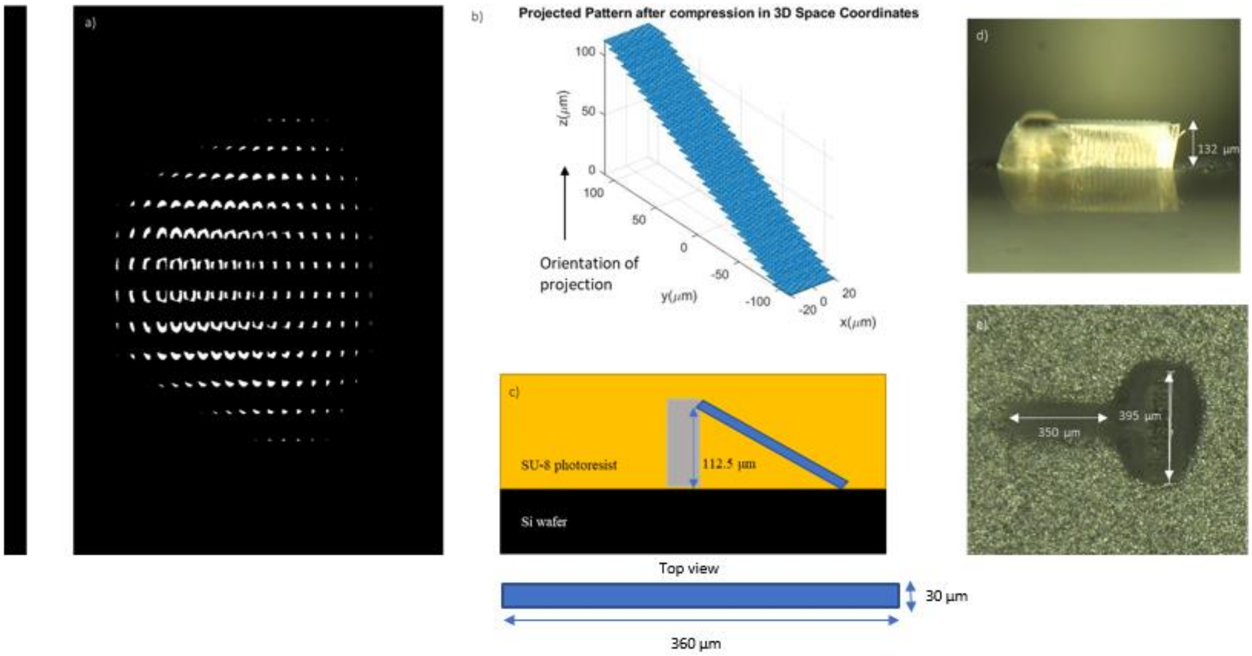

Figure 33: a) Pixel value map on the SLM to project the designed 3D structure. b) Voxel map of the designed tilted line structure after compression in real 3D coordinate. c) Illustration of the location of the projected 3D pattern inside the SU-8 photoresist. d) Photolithography result of tilted line (side view) e) Photolithography result of the tilted line (top view)

For our DMD-based 3D light field projection system, the rays after passing through the focal plane of the MLA can intersect at locations other than the designed voxels. These unexpected intersections can form unwanted voxels with fewer rays than the number of rays used for a designed voxel location. As long as there are more rays at each voxel location, our 3D pattern is cured more strongly than the unexpected voxels with fewer rays in the case of single photon absorption. However, the same reasoning cannot be applied for two-photon absorption because all designed voxels will not be cured with two-photon absorption of 520 nm fs light source. The voxel to pixel mapping scheme used for single-photon absorption determines all possible rays that can intersect at a particular voxel. All these rays have different optical path lengths and will not arrive at the same time. However, for two-photon absorption to occur, the light rays virtually need to arrive simultaneously. The photon absorption coefficient of SU-8 is proportional to the intensity of the incident photon. When two photons have the same path length and arrive at the same time, the local intensity is increased to the extent that two photons are absorbed simultaneously to cure the voxel. When all the rays are used, only symmetric rays with equal path lengths will cure the voxel in the case of two-photon lithography. Adding extra rays other than symmetric rays will not cure the voxel and will only contribute to the formation of unexpected voxels. Hence designed voxels are not cured strongly than the unexpected voxels, which is evident from these preliminary two-photon lithography results. As shown in *Figure 34*, rays can intersect at different locations other than the voxel points. Only a few of those intersection locations with symmetric rays are cured due to two-photon absorption. The unexpected voxels plot for two concentric circles at different depths and a single plane of voxels are shown in *Figure 35*. Hence to accommodate two-photon absorption effects in our 3D light field lithography system, we must improve our old voxel generation method, discussed in the following section.

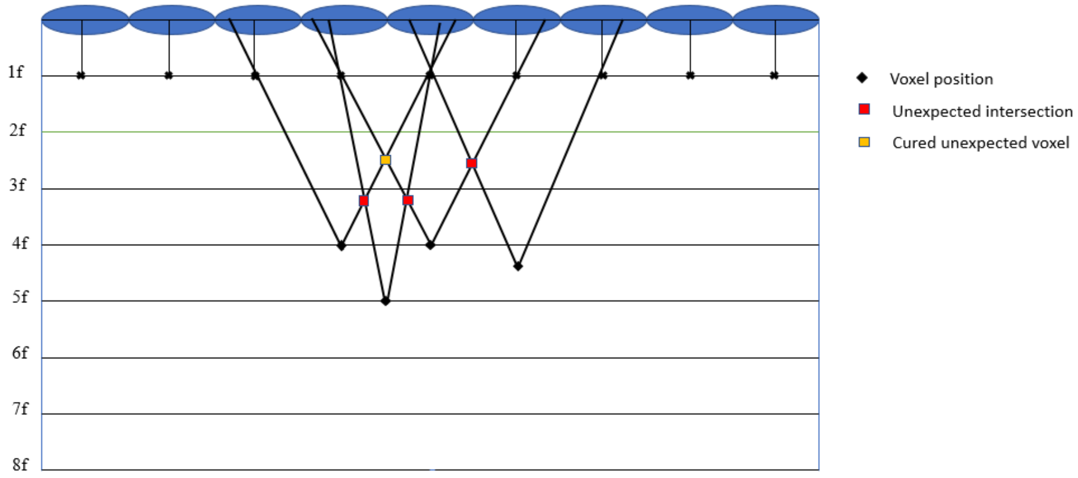

Figure 34: Simple illustration of unexpected voxel formation for a set of random voxel points

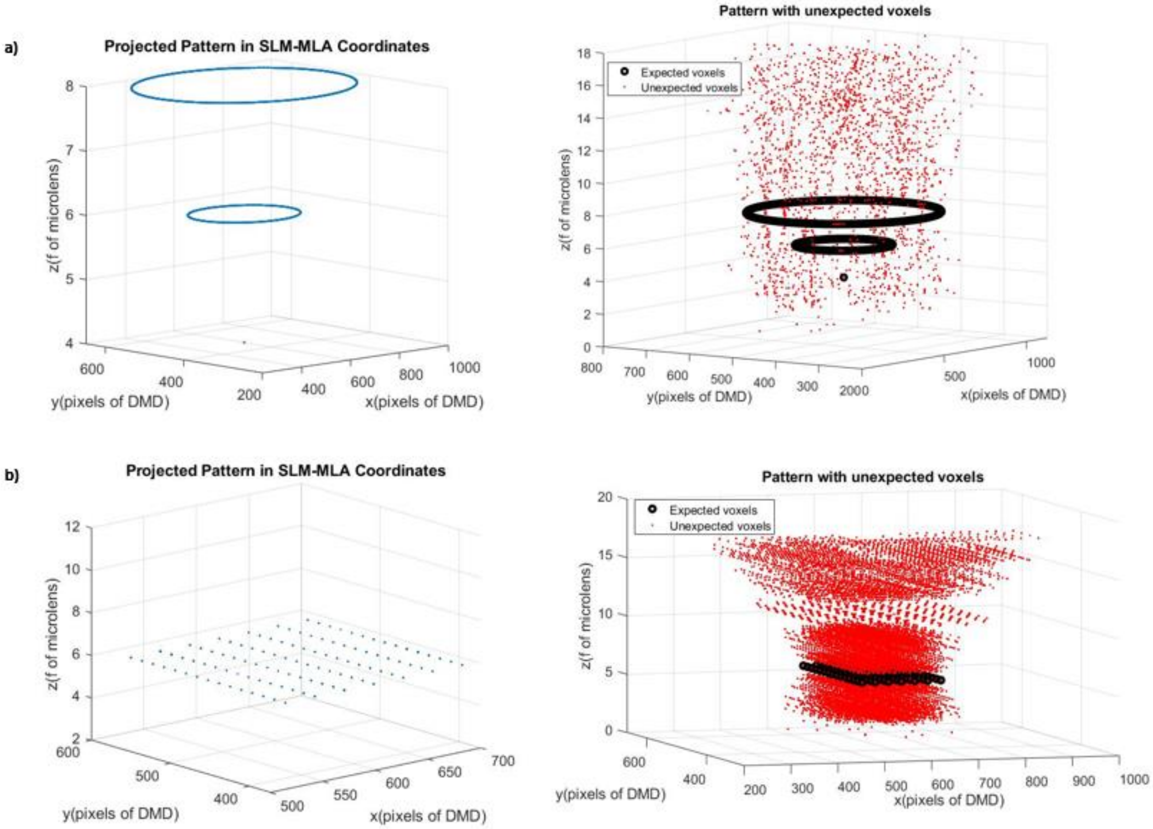

Figure 35: a) Plot of unexpected voxels formation for two concentric rings at different z positions. b) Plot of unexpected voxels formation for voxels on the single z plane

4.3. New voxel generation method

As discussed in the previous section, it is required to find symmetric rays for any designed voxel location to achieve two-photon absorption. This needs the voxel positions to be symmetric with respect to MLA. In other words, only certain voxel locations within a single micro lens can definitely have symmetric rays. From the geometry, it can be seen that only center, corner, and edge voxel locations will have symmetric rays. Hence, there can be nine such voxel positions within a single microlens, as shown in *Figure 36*. Even though rays intersect at other arbitrary locations, most of these rays are not symmetric compared to these nine voxel locations. Having such random voxel positions can generate more unwanted voxels than desired voxels which causes deviation from the design. For these symmetric lateral voxel locations, unexpected voxels can be formed along with expected voxels, as shown in *Figure 36*.

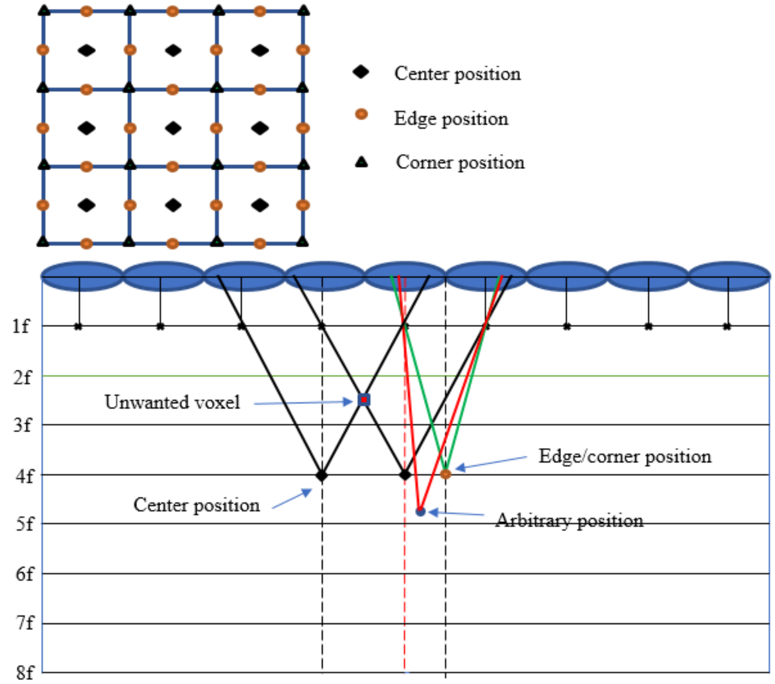

Figure 36: Symmetric lateral voxel positions within a single microlens

For obtaining symmetric rays, it is required to position the pixels within each microlens symmetrically. This is achieved when we have the same number of pixels within each microlens. The size of each microlens or the distance between two consecutive MLA boundaries is 300 µm, and the length of each diamond pixel along the diagonal is 10.8 µm. For a 1:1 magnification in the optical relay, we can have 27.778 pixels between two consecutive MLA boundaries. It is easy to ensure we have the same number of pixels within all microlens when the number is an integer. For this, we choose the closest integer, which is 28 pixels within each microlens. To obtain 28 pixels, we de-magnify the relayed SLM image by 0.9920(27.77/28), as shown in Figure 37. We use a zoom lens arrangement in the first telecentric lens pair to achieve such small magnification, as shown in *Figure 38*. A zoom lens is a mechanical assembly of multiple lens elements whose focal length can be varied instead of a fixed focal length (FFL) lens.

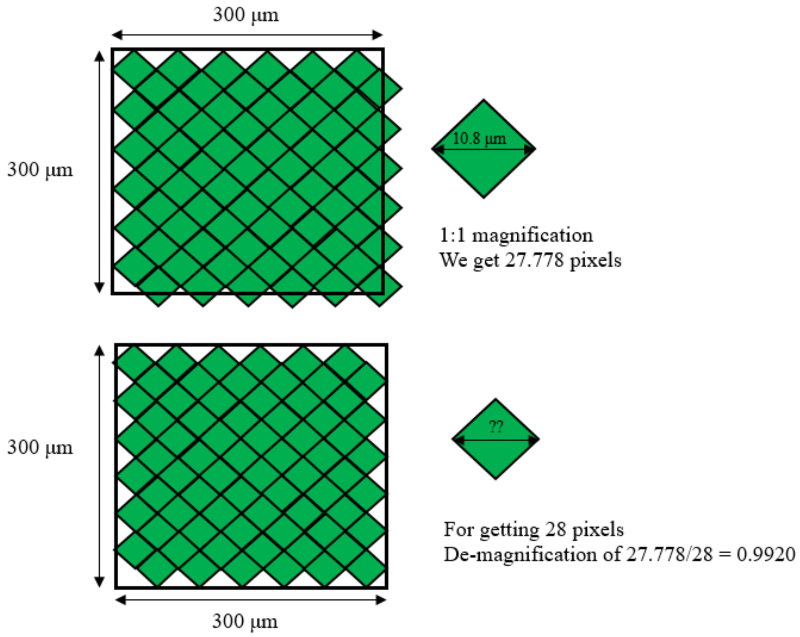

Figure 37: De-magnification of SLM pixel map to obtain 28 pixels within a single microlens

Since the magnification ratio of a telecentric lens pair is

$$m = \frac{f_2}{f_1} = 0.9920 \tag{27}$$

The effective focal length of the first compound lens arrangement of two convex lenses of focal length f_a and f_b separated by distance d_1 is given by

$$\frac{1}{f_1} = \frac{1}{f_a} + \frac{1}{f_b} - \frac{d_1}{f_a f_b}$$

$$\frac{1}{f_2} = \frac{1}{f_a} + \frac{1}{f_b} - \frac{d_2}{f_a f_b} \tag{28}$$

With the known value of f_1 the value of f_2 can be found out using the equation (27). This value of f_2 is substituted in the other Gullstrand equation (28) to find d_2. The distance between the lenses in the second compound lens arrangement is increased by adding an adapter of size d'. In that case, $d_2 = d_1 + d'$.

The effective focal length is measured from the principal planes of the combined lens system. The principal planes H_1 and H_2 for a compound lens arrangement separated by a distance are determined by the principal plane locations of individual lenses, which the manufacturer provides. Experimentally, the principal plane of the compound lens is also verified by focusing light from infinity onto a screen at a distance of f_1 or f_2. The first stage of the telecentric lens pair is then setup where the iris is at a distance of f_1 from the front compound lens and distance f_2 from the rear compound lens.

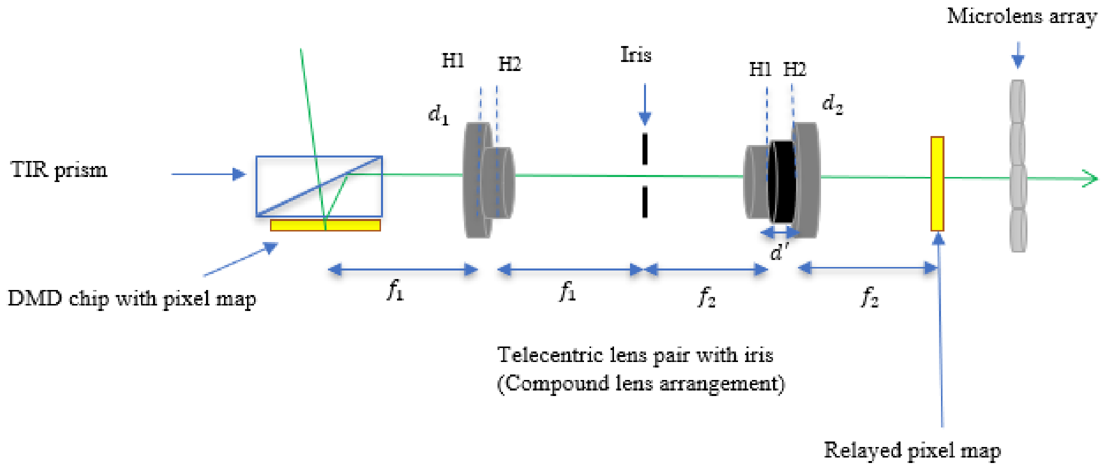

Figure 38: Zoom lens arrangement in the first telecentric lens pair system

Even after choosing the correct voxel positions and corresponding symmetric rays, it was observed that the curing was strong at discrete z locations within our 3D patterns. This is due to strong two-photon absorption at specific z locations where the intensity of light rays is maximum. When a pixel position is calculated for an arbitrary voxel in 3D space through ray-tracing methods, the calculated position might not always correspond to the center of the pixel. The pixels are finite-sized, and light emitted from the center of the pixel has the maximum intensity. Hence the voxel locations cured by these rays are stronger compared to other voxels in the vicinity. Ideally, for our design, the DMD should comprise millions of pixels, with each pixel having the maximum intensity to cure all z locations uniformly in 3D space. But due to the finite size of a DMD pixel, only discrete z locations are used to design a pattern. In other words, there is a minimum z separation distance (z_{min}) for voxels to be formed individually by two consecutive pixel centers. Any voxel between these two voxels can still be cured but with less intensity compared to the two voxels.

A pixel to voxel mapping is required to find all possible voxel z locations formed by discrete diamond pixels in DMD. Since DMD pixels are diamond-shaped, diamond indexing is followed to determine the center of each pixel, as shown in *Figure 39a*. Having an even number of pixels (28) within a microlens means the center of the microlens corresponds to the center of 4 diamond pixels which is the (0,0) position. By traversing half pixel width in both x and y directions, any arbitrary position (i, j) corresponds to the center of a diamond pixel if $i + j$ is odd as shown in *Figure 39b*. We find all the possible z locations in 3D space for the nine symmetric (x, y) voxel locations within a single microlens. For the simplest case of center position as shown in *Figure 40*, the center of an arbitrary microlens (x_c, y_c) is x_c pixels in the horizontal direction and y_c pixels away in the vertical direction from the main microlens.

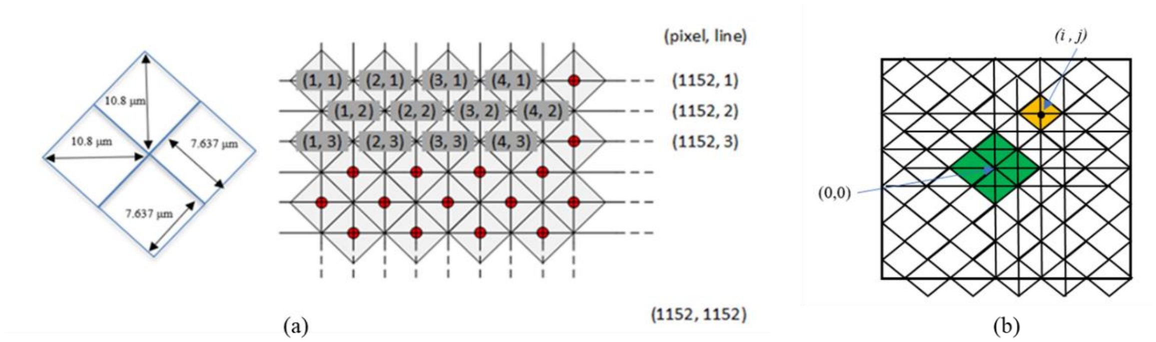

(a)

(b)

Figure 39: (a) Diamond pixels arrangement in the DMD. (b) Illustration of diamond indexing for an integer number of pixels within a single microlens

The ray travels parallel to the optical axis and hits the respective microlens, and passes through its $1f$ location. (x_p, y_p) is the total pixel distance (in pixels) from the center of the main microlens, as shown in *Figure 40*.

The final z position αf is determined by intersecting the ray with a line passing through (x_v, y_v) and parallel to the z-axis where (x_v, y_v) is the position of voxel within the center microlens. (x_v, y_v) is also changed to edge and corner positions to get the respective allowed z locations for these voxel positions.

$$\alpha f \ = \frac{\sqrt{(x_p - x_v)^2 + (y_p - y_v)^2}}{\sqrt{(x_p - x_c)^2 + (y_p - y_c)^2}} \tag{29}$$

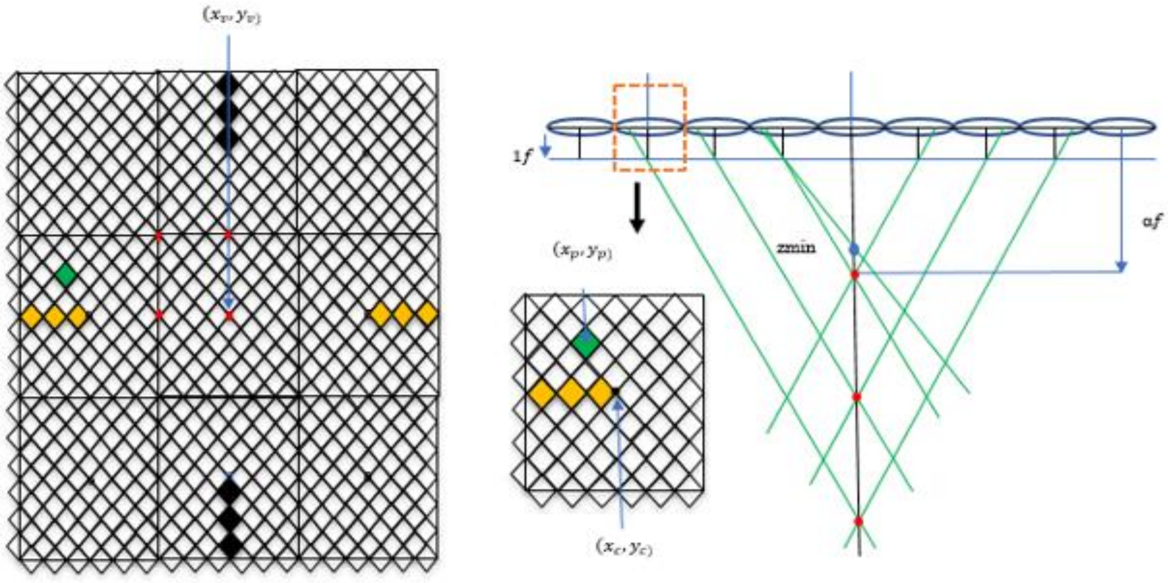

Figure 40: Pixel to voxel mapping algorithm to determine the allowed z locations for voxels within a single microlens

With our old voxel generation method, the number of rays available for each voxel increases as the z depth increases. This is because more active microlenses are available as the z depth of the voxel increases. All these rays arrive at voxel locations at different angles and are more suitable for single photon absorption. Using the new voxel generation algorithm discussed for two-photon absorption, it is found that the number of rays does not increase as the z depth increases. Only 4, 8, or at most 12 rays (for unique z locations) with the same angle and optical length are available for a voxel at any given z location.

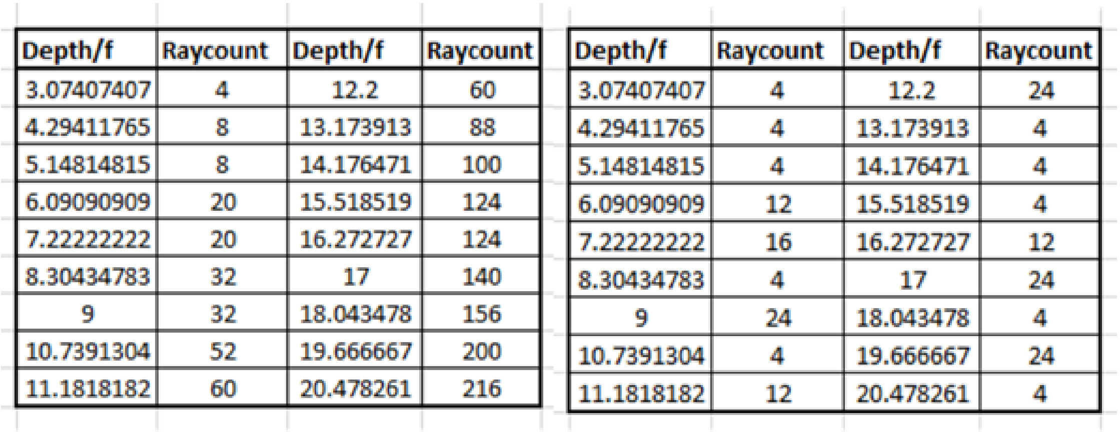

Depth/f	Raycount	Depth/f	Raycount
3.07407407	4	12.2	60
4.29411765	8	13.173913	88
5.14814815	8	14.176471	100
6.09090909	20	15.518519	124
7.22222222	20	16.272727	124
8.30434783	32	17	140
9	32	18.043478	156
10.7391304	52	19.666667	200
11.1818182	60	20.478261	216

a)

Depth/f	Raycount	Depth/f	Raycount
3.07407407	4	12.2	24
4.29411765	4	13.173913	4
5.14814815	4	14.176471	4
6.09090909	12	15.518519	4
7.22222222	16	16.272727	12
8.30434783	4	17	24
9	24	18.043478	4
10.7391304	4	19.666667	24
11.1818182	12	20.478261	4

b)

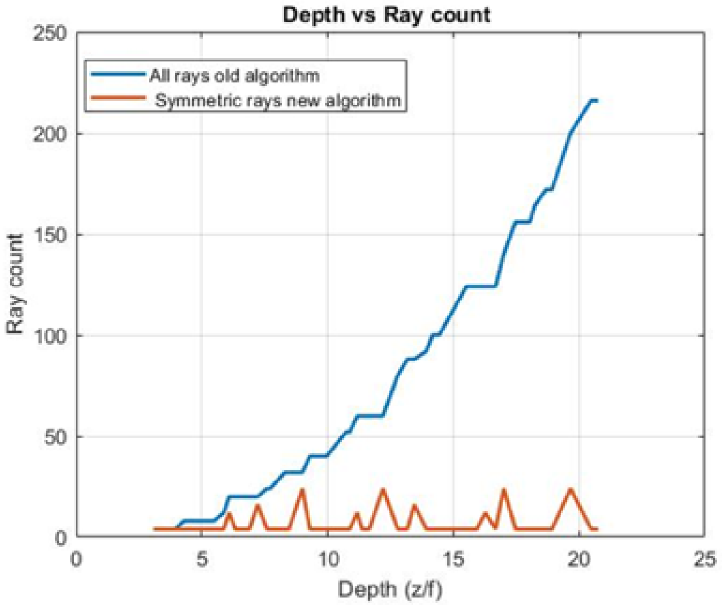

Figure 41: a) Ray count for each voxel as z depth increases for the old voxel generation method. b) Ray count for each voxel as z depth increases for the new voxel generation method.

Thus, we get fewer rays which are more accurate in our new voxel generation algorithm compared to the old one. The voxel positions with the new algorithm are now limited to only certain (x, y) positions and allowed z locations. With these limited voxel positions, a 3D object is designed and discretized into individual voxels. Only a few simple 3D patterns can be designed and fabricated with two-photon femtosecond light field lithography with less flexibility. The new algorithm reduced the number of unexpected voxels for a simple plane of voxels from 5000 to 900, as shown in *Figure 42*. This reduction is due to the fewer number of rays used to cure the 3D pattern.

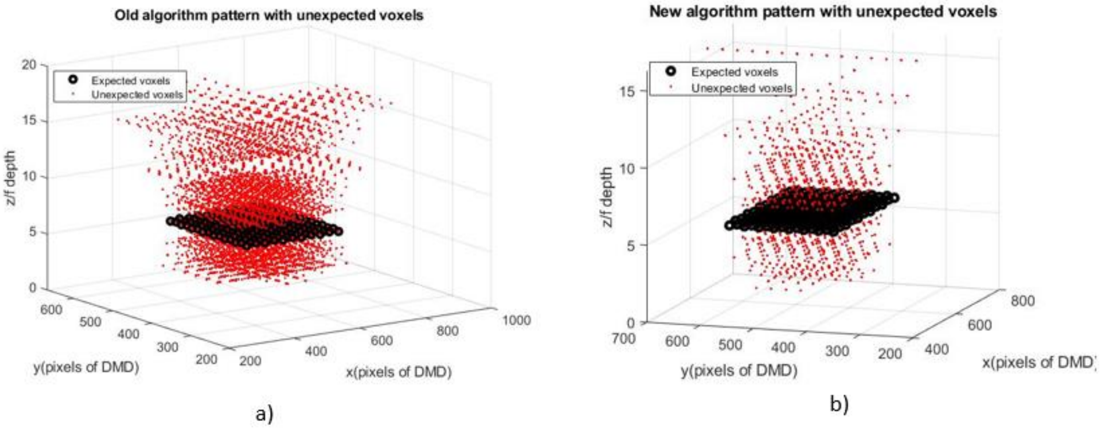

Figure 42: a) Unexpected voxels plot for a plane of voxels with the old algorithm. b) Unexpected voxels plot for a plane of voxels with the new algorithm

These unexpected voxels can be further reduced by using a simple ray deletion algorithm, as shown in *Figure 43*. For any unexpected voxel formed by two rays, the ray that already is a part of a strong voxel is given less priority and deleted. This way, all rays responsible for unexpected voxels are deleted based on prioritization. Ideally, this deletion logic should leave no rays behind, but we set a limit of at least four rays for each voxel. This means that all voxels will have at least four rays after implementing the deletion logic. The following section will briefly discuss the new SLM-MLA calibration procedure for the new improved algorithm and the results of the photolithography.

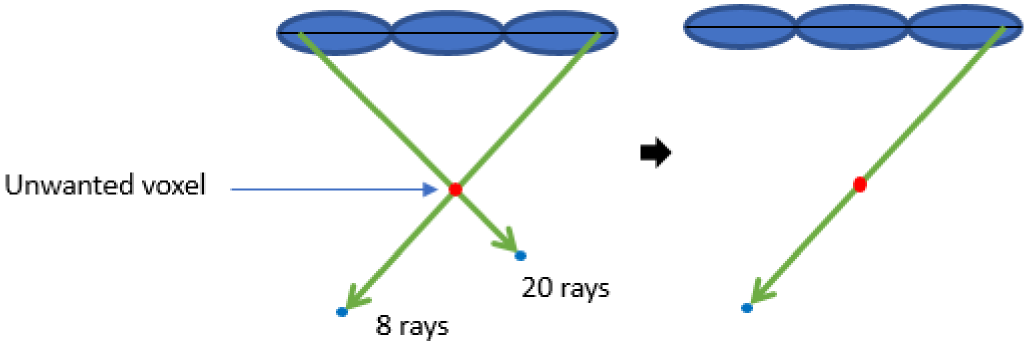

Figure 43: Illustration of deletion logic. The ray, which is part of a voxel with fewer rays, is prioritized. Hence the ray responsible for the voxel with 20 rays is deleted to remove the unwanted voxel

4.3.1. New SLM-MLA calibration

The accuracy of this 3D light field projection system entirely depends on the relative positions between the SLM and the microlens array. The SLM-MLA calibration determines the extent to which the designed structures or patterns are successfully projected onto the 3D space. The voxels can be projected accurately in 3D space only if a perfect correspondence exists between the SLM and MLA. Otherwise, the projected patterns will have undesired distortion and ghost images.

For the new voxel generation method, we require 28 pixels between the boundaries of any microlens. This requires a de-magnification of 0.9920 in the relayed pixel map after the first telecentric lens pair. It is difficult to perform such precise calibration with our previous calibration procedures discussed in [56], which is beyond the scope of the CCD camera. Hence calibration is done by adding a microscope to calibrate the DMD pixels and microlens position at a micrometer scale. We add a 5x objective lens at its working distance from the sharp relayed pixel map to magnify the pixel map. A 300 mm eyepiece lens is used to visualize the magnified image on the CCD camera, as shown in *Figure 44*.

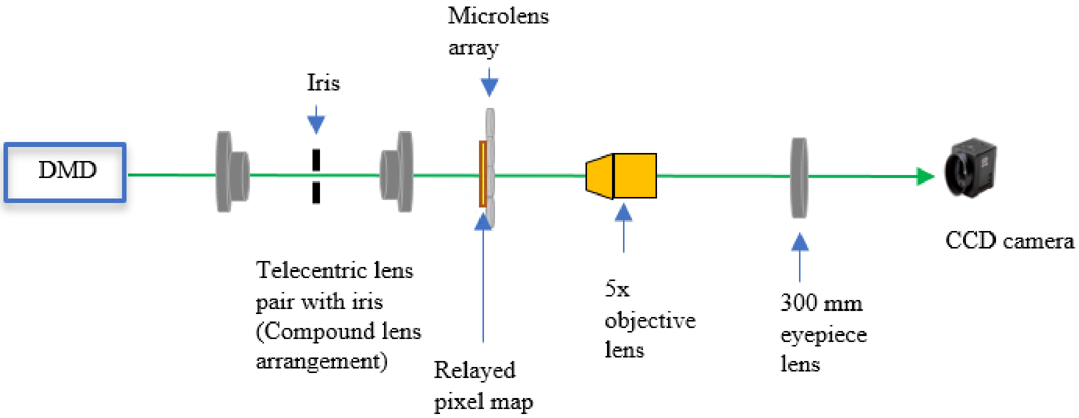

Figure 44: Schematic of calibration setup with a microscope arrangement

The first step in this calibration process is to remove the MLA from the setup and image the sharp SLM pixel map on the camera when all the pixels are turned on, as shown in *Figure 45a*. This position or plane of imaging corresponds to the $0f$ location. The diamond pixels arrangement in DMD can be verified at this magnification, and the tilt along these pixels in both directions is corrected on the camera. Then the MLA is added back into the setup and positioned at a distance of $1.1f$ from the SLM image plane at $0f$. The distance of $1.1f$ is chosen because at this configuration the lateral and depth resolution remains almost constant over our pattern projection region as discussed in chapter 3. The microscope is imaged at the plane of sharp MLA boundaries at this distance, as shown in *Figure 45b*. The corresponding distance d_1 between the MLA boundaries in *Figure 45b* is also recorded in the camera coordinate system.

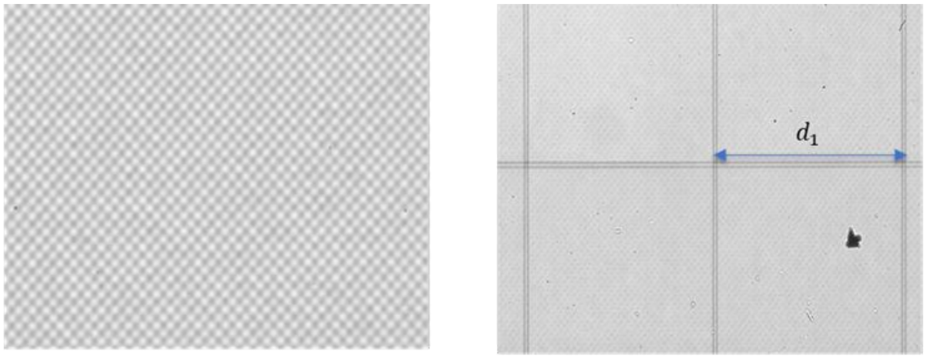

(a) (b)

Figure 45: a) Magnified image of diamond shaped DMD pixels b) Sharp magnified image of MLA boundaries at $1.1f$

The second step in this process is to verify the number of pixels between two boundaries of a microlens. As shown in *Figure 46a*, a pixel map with centerlines is projected to obtain its magnified image at $1.1f$ on the camera, as shown in *Figure 46c*. The pixels are sharp at the $0f$ location as discussed above, and the light is diverging at $1.1f$ location which gives the blurred image. Hence through linear fitting, two adjacent sharp pixel edge points are chosen, and the pixel data is extrapolated. The corresponding distance between these two sharp edge points d_2 in camera pixels is noted. The magnification ratio in the first stage telecentric lens pair is fine-tuned until the two distances d_1 and d_2 become equal. Once the arrangement is fixed, the first telecentric lens pair is not be disturbed.

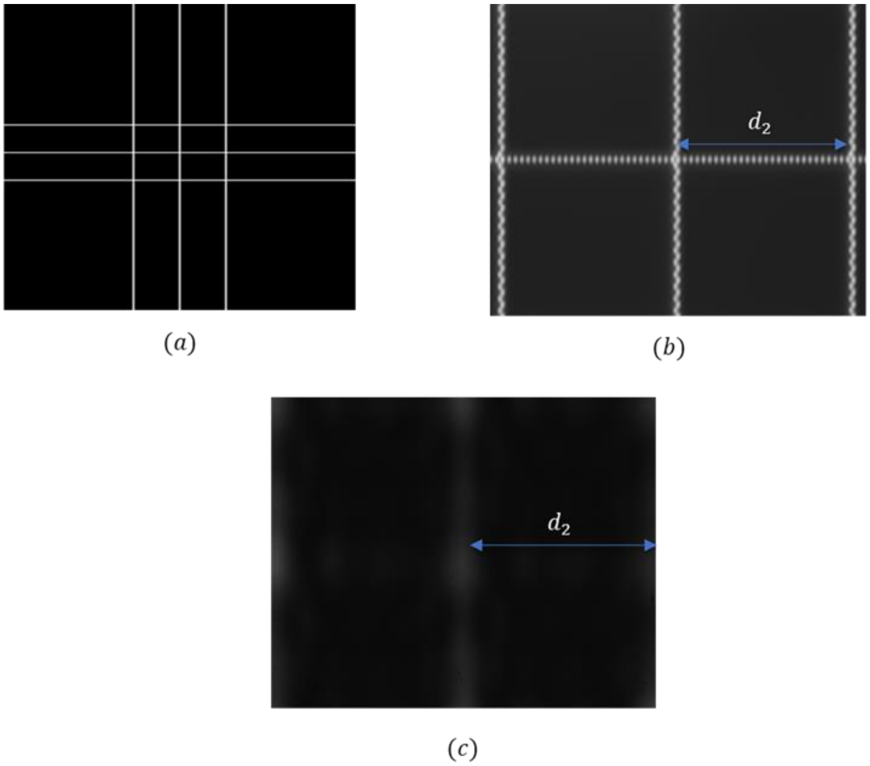

Figure 46: a) Computer-generated pixel map containing centerlines separated by 28 pixels. b) Magnified image of the centerlines at $0f$ location on camera. c) Magnified image of the centerlines at $1.1f$ location on camera

The third and final step is to adjust the MLA position with respect to the fixed DMD pixel map. This is similar to the previous step where the central pixel position in the centermost line and the central pixel position in the adjacent line separated by 28 pixels are recorded in the camera coordinate system. Lines are drawn from these positions as indicated by red and blue lines in *Figure 47*. The MLA is inserted at $1.1f$ plane as in the second step, and its (x, y) position is adjusted accordingly to match the sharp MLA boundaries on camera with these red and blue lines. The calibration procedure aims to align the center of the innermost four microlenses with the centermost pixel in the DMD and have exactly 28 pixels between two adjacent microlens boundaries. These three steps ensure perfect one-to-one correspondence between SLM and MLA to project 3D patterns accurately.

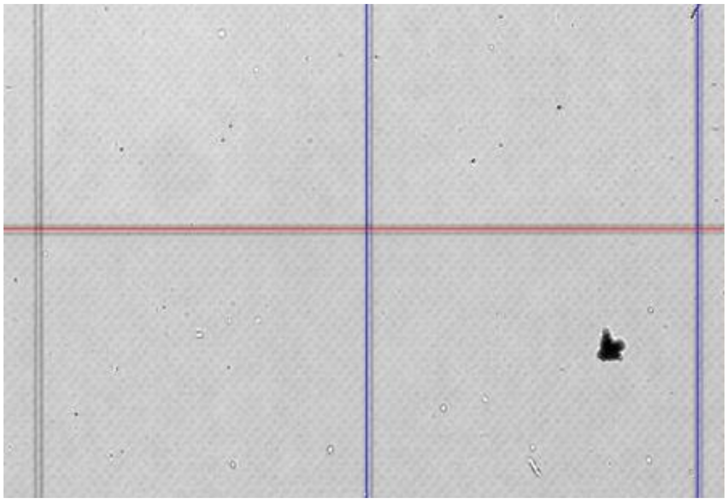

Figure 47: Adjusting MLA (x, y) position to match the red and blue lines based on SLM pixel positions on the camera

4.3.2. Photolithography results

Based on the new voxel generation method, 3D structures were designed and fabricated on a SU-8 photoresist. The first structure fabricated was plateau, as shown in *Figure 48b*. For the designed plateau, the base length was 112.5 µm, the base width was 150 µm, and the height of the plateau was 112.5 µm. The corresponding pixel value calculated from the new algorithm is shown in *Figure 48a*. The pixels along the microlens boundaries are still not used to create the voxels in the new algorithm. The pattern was exposed for 8 minutes on a thick SU-8 photoresist. The resultant fabricated pattern is shown in the figure *Figure 48d,e*. The height of the plateau structure is 118 µm which is comparable to that of our design height. The lateral size of our plateau is also in good correspondence compared to our design.

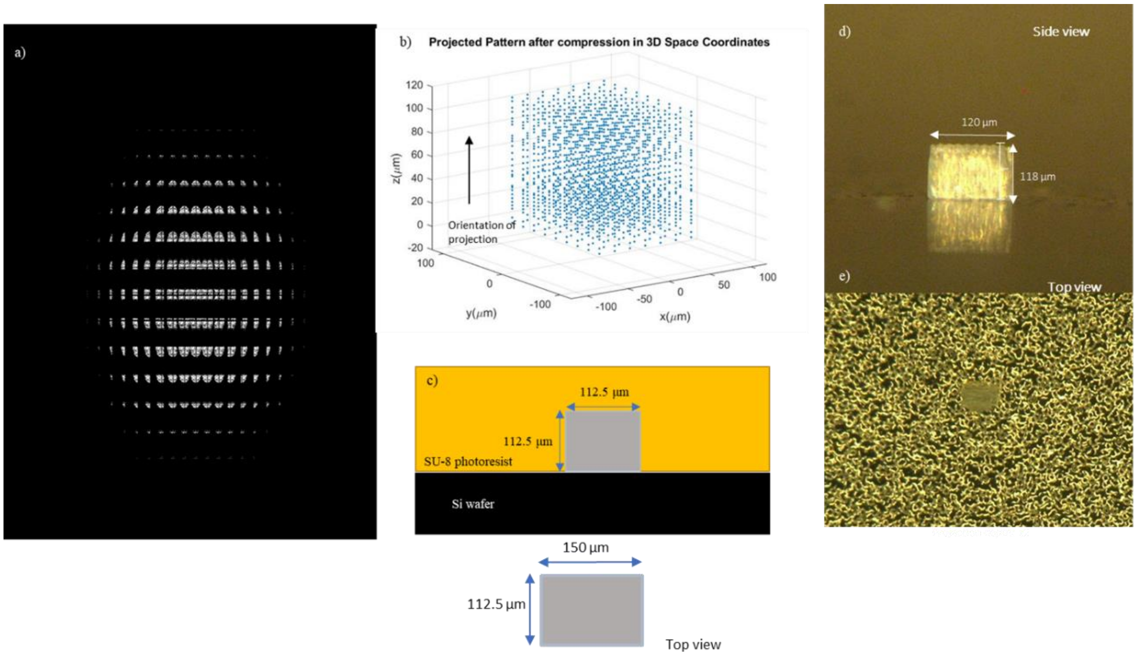

Figure 48: a) Pixel value map on the SLM to project the designed 3D structure. b) Voxel map of the designed plateau structure after compression in real 3D coordinates. c) Illustration of the location of the projected 3D pattern inside the SU-8 photoresist. d) Photolithography result of plateau structure (side view) e) Photolithography result of plateau structure (top view)

We designed and fabricated a stepped plateau structure to verify our hypothesis and validate the new voxel generation method. The stepped plateau was designed to have a height difference of 112.5 µm on one side and 56.25 µm on the other side with a steep decrease in height in the middle, as shown in *Figure 49b*. The design base length was 187.5 µm, and width was 112.5 µm. The corresponding pixel value map calculated from the new algorithm is shown in *Figure 49a*. The fabrication results show that the step function was not achieved accurately as our design. The lower step has unwanted voxels, which increases the height of our fabricated pattern. As shown in *Figure 49d,e*, the unwanted voxels are less for 8 mins of exposure compared to 12 mins which can be seen as a difference in the height. We require higher exposure times for the new algorithm because of the limited rays available for two-photon curing.

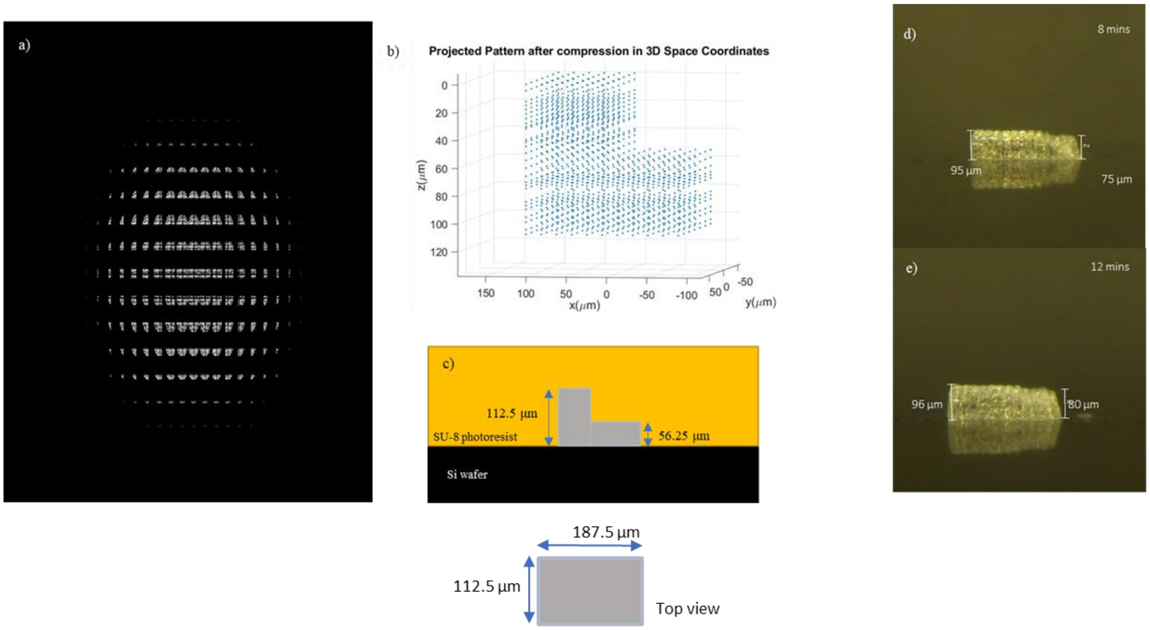

Figure 49: a) Pixel value map on the SLM to project the designed 3D structure. b) Voxel map of the designed stepped plateau structure after compression in real 3D coordinates. c) Illustration of the location of the projected 3D pattern inside the SU-8 photoresist. d)Photolithography result of the 3D pattern after 8 mins exposure (side view) e) Photolithography result of the 3D pattern after 12 mins exposure (side view)

Double tilted line (hill) 3D structure was also designed and tested to validate our new voxel generation algorithm. For the designed hill structure, the height was 56.25 µm (7f to 10f) location, and the base length was chosen to be 187.5 µm, as shown in *Figure 50b*. The corresponding pixel value calculated from the new algorithm is shown in *Figure 50a*. The pattern was exposed for 9 mins, and the fabrication results are shown in *Figure 50d,e*. The fabricated pattern's height was 75 µm which is in close relation with our design. However, the fabrication results show shape deviation from the design. The top of the hill structure is swelled due to unexpected voxels formation.

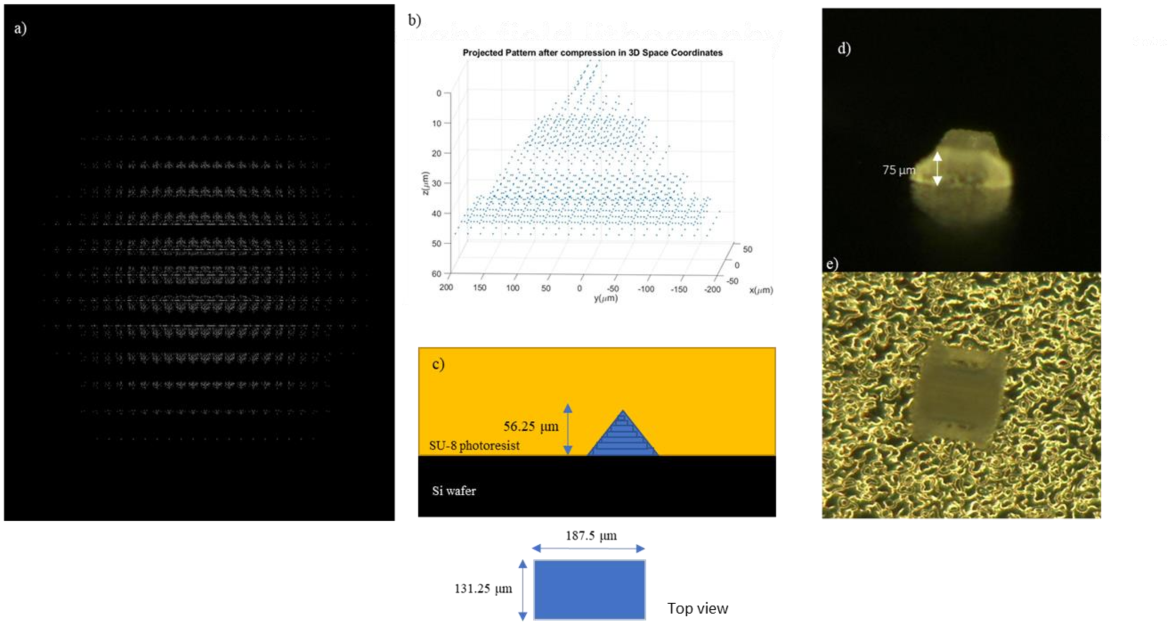

Figure 50: a) Pixel value map on the SLM to project the designed 3D structure. b) Voxel map of the designed hill structure after compression in real 3D coordinates. c) Illustration of the location of the projected 3D pattern inside the SU-8 photoresist. d) Photolithography result of the hill pattern (side view) e) Photolithography result of the hill pattern (top view)

Ray deletion logic reduces the number of rays available for our designed pattern, which sometimes is not strong enough to cure our 3D pattern but strong enough to cure unexpected voxels, as seen in these photolithography results. The unexpected voxels can also be minimized by manipulating the design. In the case of tilted lines, for a single z plane, our old design considered voxels in the same line as shown in *Figure 51a*. For this arrangement, the number of unwanted voxels is proportional to the number of voxels in the line. However, when the voxels are oriented at 45°, as shown in *Figure 51b*, there will be no unexpected voxels. The number of unwanted voxels for a tilted line at 0° orientation and 45 ° orientation is shown in *Figure 51*. This tilted line design will form no or very few unwanted voxels.

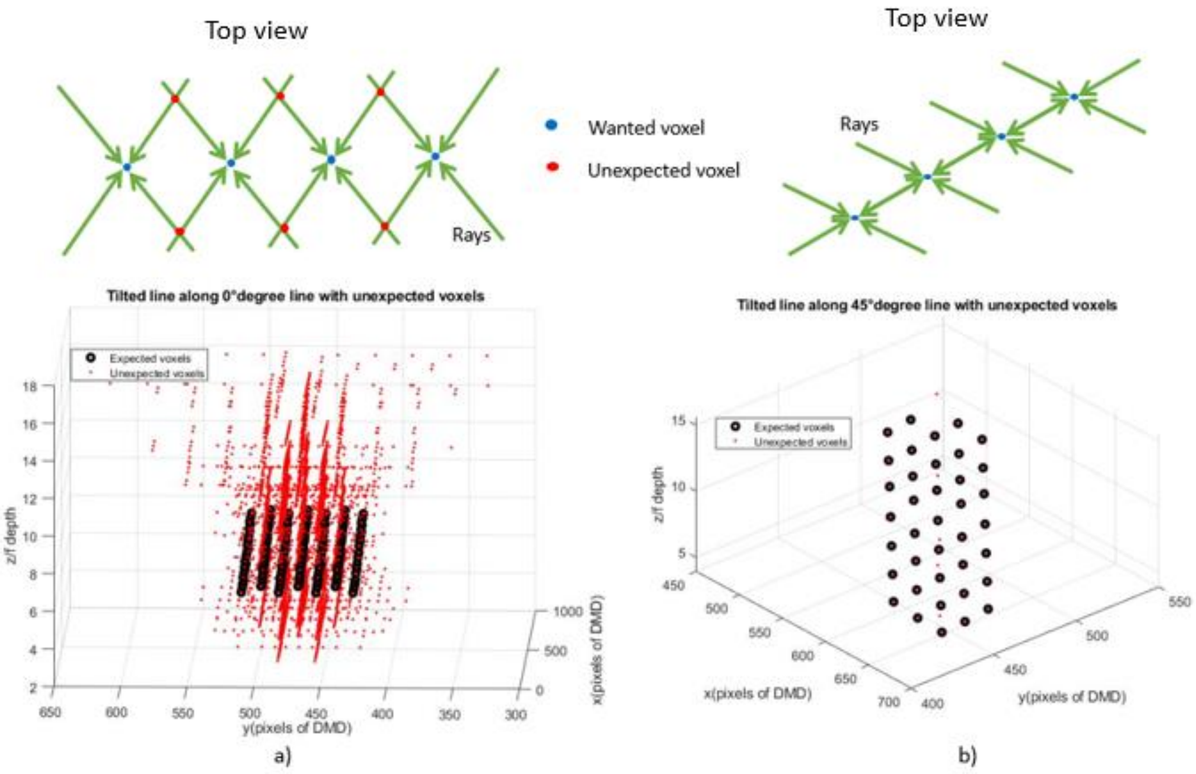

Figure 51: a) Unwanted voxels plot for a tilted line where voxels are oriented at 0° b) Unwanted voxels plot for a tilted line where voxels are oriented at 45°

A tilted line from this new design was projected and patterned on the photoresist to verify our hypothesis. The designed tilted line at 45° orientation is shown in *Figure 52b*. The height of the design is 131.25 µm, and the line is two microlenses wide 56.25 µm. Since this design has very few unwanted voxels, more unsymmetric rays are also added to increase the curing rate at voxel locations. In addition to this, more rays are added as z depth increases to compensate for the loss in the intensity. The pixel value map for this structure is shown in *Figure 52a*. The pattern was exposed for 8 mins, and the fabrication results are shown in *Figure 52d,e*.

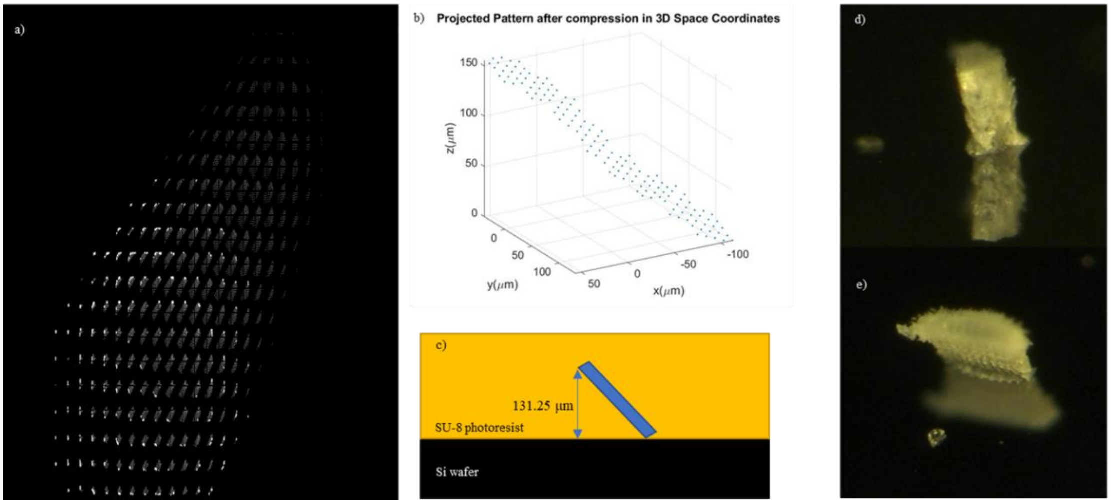

Figure 52: a) Pixel value map on the SLM to project the designed 3D structure. b) Voxel map of the designed tilted line at 45°after compression in real 3D coordinates. c) Illustration of the location of the projected 3D pattern inside the SU-8 photoresist. d) Photolithography result of the new tilted line pattern (side view) e) Photolithography result of the new tilted line pattern (angled view)

The results indicate that unexpected voxels are cured strongly compared to the designed voxels, irrespective of the design. The reason for this strong curing is that our 3D projection location is closer to the $1f$ plane. The strongly cured unwanted voxels change the final shape of our fabricated structure. For most of our patterns, the z projection location was fixed from $6f$ to $12f$. The unwanted voxels are formed closer to the $1f$ plane of maximum intensity. When a voxel at $6f$ plane requires n rays, each of these n rays can strongly cure unexpected voxels at $2f$ and $3f$ planes. Due to the MLA, light rays focus at $1f$ plane and constantly diverge as z depth increases. This decreases the intensity of light rays proportionally as z depth increases. When the projection location is shifted farther away from the strong $2f$ and $3f$ planes, for instance, $10f$ to $20f$, the effect of unwanted voxels becomes less dominant near the projection location. When a voxel at $12f$ plane requires n rays, only a few of these n rays are strong enough to cure unexpected voxels at nearby planes of $6f$ and $7f$. The unwanted voxels are still stronger near the $2f$ and $3f$ planes, but the z location of our photoresist can be adjusted to project these strong planes outside. The location of the unexpected voxels determines the strength with which they are cured. Reducing the number of unwanted voxels at $3f$ and $4f$ plane using deletion algorithm will still cure our pattern and cause shape deviation.

To verify and validate our hypothesis, tilted line structures were designed and projected from the $10f$ plane to $20f$ plane as shown in *Figure 53b*. The wavelength of the femtosecond light source was changed from 520 nm to 405 nm and 415 nm because it was desired to observe single-photon absorption along with two-photon absorption. Given that our projection location is farther away from the strong regions of unexpected voxels, it was expected that single-photon absorption would not cause any significant changes to our cured pattern. Additionally, more un symmetric rays were added to compensate for the reduced intensity of light at such deep locations. Since light is constantly diverging with increasing z depth, the light intensity at $10f$ to $20f$ planes is low, requiring more rays with higher exposure times. The pixel map for this 3D pattern was created by considering all these factors and is shown in *Figure 53a*. The pixel map was then loaded into the SLM to expose the pattern for various minutes. The resultant fabricated pattern for 405 nm is shown in *Figure 53d,e,f*.

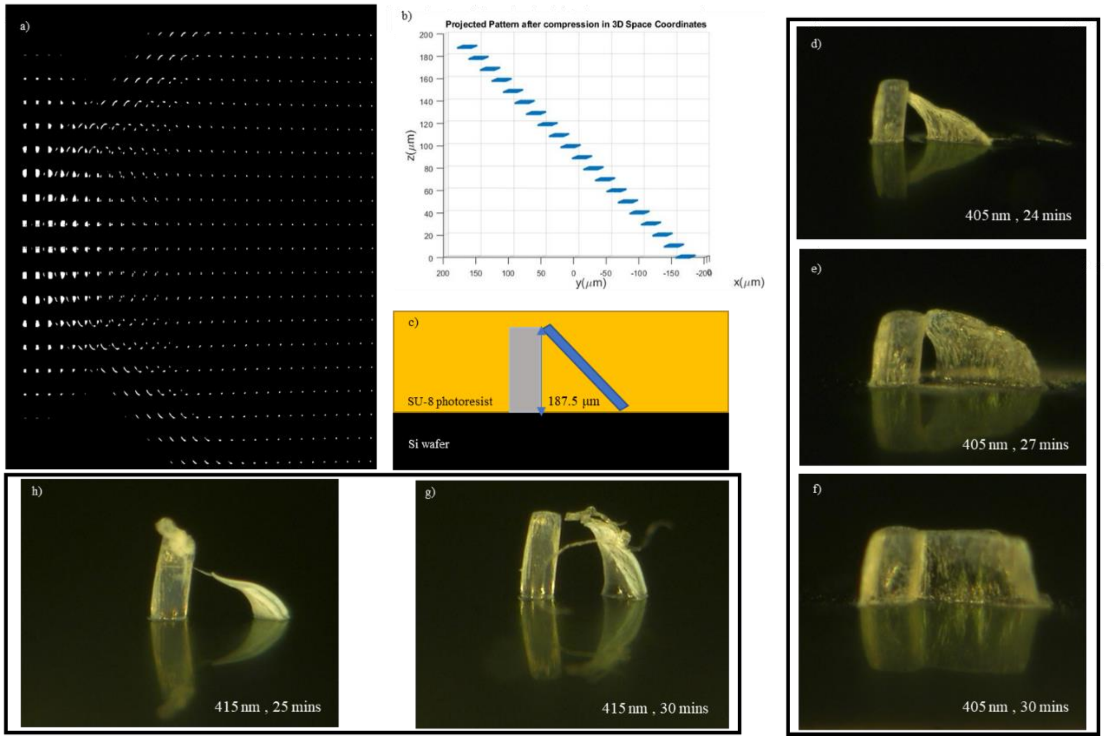

Figure 53: a) Pixel value map on the SLM to project the designed 3D structure. b) Voxel map of the designed tilted line at 10f to 20f after compression in real 3D coordinates. c) Illustration of the location of the projected 3D pattern inside the SU-8 photoresist. d) 405 nm photolithography result of the designed pattern for 24 mins exposure (side view) e) 405 nm photolithography result of the designed pattern for 27 mins exposure (side view) f) 405 nm photolithography result of the designed pattern for 30 mins exposure (side view) g) 415 nm photolithography result of the designed pattern for 30 mins exposure (side view) h) 415 nm photolithography result of the designed pattern for 25 mins exposure (side view)

From the results for 405 nm wavelength, it can be verified that our fabricated pattern has good shape correspondence with our design. The tilt of the line is best visible with respect to the straight wall for 24 mins exposure. Increasing the exposure time from 24 minutes to 27 mins will form a thick plateau-like tilted line filled with some unexpected voxels. Increasing the exposure time further to 30 mins will form a complete plateau like structure with lot of unexpected voxels. However, minimum exposure time (~ 20 mins) is required to cure this pattern at such deep locations. Using exposure times lower than the threshold formed weak patterns which got washed away during development. The results for 415 nm wavelength, shown in *Figure 53 g,h*, are also similar to 405 nm results with a good shape correspondence to our design.

In our previous test results for projections at $6f$ to $12f$, we could see that our results were inevitably dominated by unexpected voxels. Irrespective of the exposure time, unexpected voxels are cured strongly in the $2f$ to $4f$ planes, which controlled the final shape output of our fabrication. Shifting the projection location from $10f$ to $20f$ caused the patterns to be cured faster than the unexpected voxels near our pattern for a proper exposure time. The strong regions of unexpected voxels were far away from our projection location to alter the final shape of our fabrication.

Although our results show good correspondence, the lack of intensity at those deep z locations requires higher exposure times. This is inherently a limitation with our DMD type SLM and MLA 3D light field projection system. To have maximum intensity at every voxel location along the z-direction without any diverging effects, we propose to use a phase-only type SLM in the future. This type of SLM does not require an MLA, and the intensity of rays does not depend on the voxel location in 3D space. In the next section, we will summarize the findings in this thesis regarding our two-photon 3D light field lithography and briefly introduce the concepts of our new phase-only type SLM and how it can overcome the limitations of our current 3D projection system.

5. CONCLUSIONS AND FUTURE WORKS

The main focus of this thesis was to explore the limits of our in-house DMD-based 3D projection system to achieve two-photon lithography. Based on our successful demonstration of single-photon 3D light field lithography results in the past, we switched to a 405 nm, 415 nm and 520 nm femtosecond laser source to prevent unwilling curing along the path of the rays and harness two-photon absorption effects at the voxel locations. Our preliminary test results for two-photon 3D light field lithography revealed that the final fabricated structures have deviations from the design in the form of unwanted voxels. To solve and improve our fabrication results at each step, a study was carried out in this thesis to understand and hypothesize all possible reasons for this mismatch.

It was summarized in this thesis that the limitations associated with our DMD-based light field projection system arise from the fact that it is not the exact inverse process of light field imaging. Light can only be sent parallel to the optical axis, and the angle of rays coming from each DMD pixel cannot be controlled individually. After passing through the MLA, these light rays focus at the 1f plane and constantly diverge along with z depth. This reduces the intensity of rays available at deep z locations for curing and increases the voxel size. Unexpected voxels are inevitably a limitation with this DMD and MLA-based 3D projection system. Even though designing 3D structures with appropriate ray selection and deletion algorithms can minimize the number of such unexpected voxels, as discussed in the thesis, these voxels are formed with much higher intensities closer to the focal plane. Such strongly cured unexpected voxels can manipulate the final fabricated structure. Moving the projection location from $6f - 12f$ to $10f - 20f$ improved the lithography results due to the formation of relatively weak unexpected voxels before the projection location. However, the projection location being far from the MLA makes the light diverge more and weakens the 3D projections. Thus, more compensation rays are required with a higher exposure time. Overall it can be concluded that our two-photon 3D light field lithography system has the capability to perform large-area 3D microfabrication within a short amount of time.

In our current DMD system, light focuses and diverges continuously before reaching the intended voxel locations. Since two-photon absorption can precisely cure any point within our photoresist with high resolution, it is crucial to ensure that the intensity does not vary with the z location and is maximum at all voxel locations to cure the 3D patterns uniformly. The way to achieve such directional steering of light rays from each pixel is by using a phase-only type SLM over our current amplitude only DMD type SLM.

For our future work, we propose using Liquid Crystal on Silicon (LCoS) reflective-type phase-only spatial light modulator (HOLOEYE GAEA 2) to project 3D patterns directly without using MLA like in our current system. This new type of SLM works based on a special state of matter known as Liquid crystals (LCs). These liquid crystals are elliptical elongated rod-like organic molecules that exhibit unique properties from both solids and liquids. At high temperatures, LCs are randomly oriented as in the liquid state, but under specific conditions, all the molecules align themselves in a preferred direction to form dipoles that react to an external electrical field. Depending on the applied external stimuli, LCs can have different molecular orientations. These binding forces within each LC are stronger in a preferred crystalline direction which forms birefringent materials. In these materials, the variation in refractive index is maximum along the long axis of orientation, also known as the extraordinary axis. Due to this variation in refractive index, the phase velocity of the wave propagating via these LCs varies depending on its polarization.

This type of SLM is a pixelated display formed by thousands and thousands of LC-filled cells. Each cell's molecular alignment can be controlled independently through externally applied voltage. Under normal conditions with no externally applied voltage, the molecules tend to orient in the preferred directions, but in the presence of an external electric field V, the molecules tend rotate by an angle $\theta(V)$. As result, the refractive index along the long axis $n_e(\theta)$ decreases in proportion with ordinary refractive index n_o

$$\frac{1}{{n_e}^2(\theta)} = \left(\frac{cos\theta}{n_e}\right)^2 + \left(\frac{sin\theta}{n_o}\right)^2 \tag{30}$$

As a result, the device acts as a digital phase retarder which retards the phase of the incoming wave $\Delta\emptyset(V)$ depending on the applied voltage V

$$\Delta\emptyset(V) = \frac{2\pi}{\lambda}(n_e - n_o)d \tag{31}$$

where λ is the wavelength of light and d is the thickness of LC. When a linearly polarized input light field is used, only the component of polarization parallel to the long or extraordinary axis acquires a phase shift with the amplitude remaining the same [57].

The voltage can be controlled using grayscale images, usually, an 8-bit encoder allowing 256 colors. This type of SLM has 10 megapixels (4160 x 2464), where the phase of each pixel or LC cell can be controlled individually by encoding a desired phase pattern on the SLM. The phase pattern is computer-generated by giving the input pixel values, which the SLM converts to an expect phase value. The pixel value of 0 would be 0 phase, the pixel value of 255 would be 2π phase, and a pixel value of 127 would be 1π phase. Regardless of the phase pattern added to the

SLM, whether it is a lens function or a blazed grating function, pixel values from 0 - 255 would always be converted linearly to phase ranging from 0 - 2 pi. A schematic representation of the LCOS-based SLM is shown in *Figure 54*.

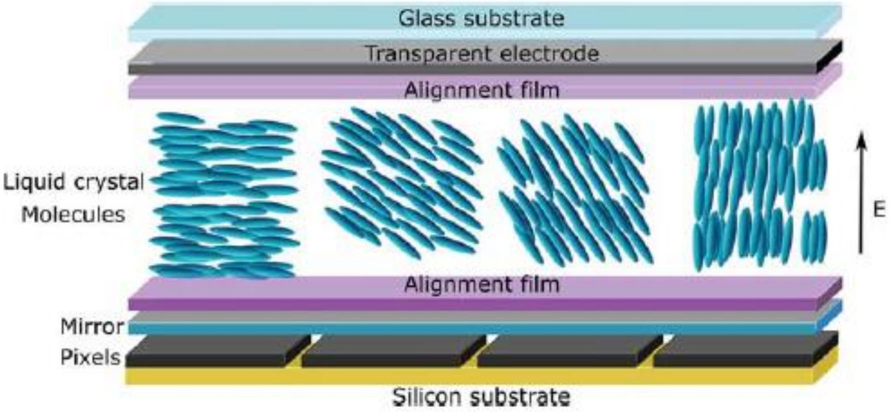

Figure 54: Schematic representation of LCoS SLM. Liquid crystal cells sandwiched between alignment films and transparent electrodes. Silicon substrate is present in the bottom surface over which an active circuit is directly connected to pixelated metal electrodes that control the orientation of LC molecules within each pixel. Reprinted from [57]

The phase patterns for the new SLM are computer generated by alternating the pixel intensity values constantly from 0 to 255 to have constant change in phase values to reflect light at different voxel locations. A sample phase pattern is shown in *Figure 55*.The new SLM is loaded with these phase patterns, and light is reflected from the SLM to form 3D patterns in real space. In the case of two-photon lithography, this SLM solves a significant limitation of choosing symmetric rays. Unlike our current system with DMD and MLA, a circular band of pixels can be given the same phase value in a phase-only type SLM for us to have precise and strong two/multiphoton absorption. Additionally, all these rays can focus and have maximum intensity at the respective voxel locations.

The new phase-only SLM can also form unexpected voxels like in our current system. Voxels on the same z plane can have pixels with identical phase values, resulting in unexpected voxels. However, due to the symmetry of DMD and MLA in our current system, we find 4 -10 symmetric rays with equal path lengths for a voxel. The unexpected voxels, in this case, are also formed by 4 rays which means that when a wanted voxel is created, it is almost certain that unwanted voxels are also formed along with it. For the future SLM, we can have as many rays as we want for a voxel because the phase value of the pixel decides the path length of the rays. As our immediate future step, we will be switching to this new phase-only type SLM and use the same 520 nm femtosecond laser to project and fabricate simple 3D microstructures and later move on to complex fabrications.

Figure 55: A sample computer generated phase pattern for the new SLM.

REFERENCES

[1] G. Postiglione, G. Natale, G. Griffini, M. Levi, and S. Turri, “Conductive 3D microstructures by direct 3D printing of polymer/carbon nanotube nanocomposites via liquid deposition modeling,” *Compos. Part A Appl. Sci. Manuf.*, vol. 76, pp. 110–114, 2015, doi: 10.1016/j.compositesa.2015.05.014.

[2] V. Sundararaghavan and N. Zabaras, “Classification and reconstruction of three-dimensional microstructures using support vector machines,” *Comput. Mater. Sci.*, vol. 32, no. 2, pp. 223–239, 2005, doi: 10.1016/j.commatsci.2004.07.004.

[3] T. Betancourt and L. Brannon-Peppas, “Micro-and nanofabrication methods in nanotechnological medical and pharmaceutical devices,” *Int. J. Nanomedicine*, vol. 1, no. 4, pp. 483–495, 2006, doi: 10.2147/nano.2006.1.4.483.

[4] M. D. Sarker, S. Naghieh, N. K. Sharma, and X. Chen, “3D biofabrication of vascular networks for tissue regeneration: A report on recent advances,” *J. Pharm. Anal.*, vol. 8, no. 5, pp. 277–296, 2018, doi: 10.1016/j.jpha.2018.08.005.

[5] H. Zhang, J. K. Jackson, and M. Chiao, “Microfabricated Drug Delivery Devices: Design, Fabrication, and Applications,” *Adv. Funct. Mater.*, vol. 27, no. 45, pp. 1–31, 2017, doi: 10.1002/adfm.201703606.

[6] C. D. Lindsay, J. G. Roth, B. L. LeSavage, and S. C. Heilshorn, “Bioprinting of stem cell expansion lattices,” *Acta Biomater.*, vol. 95, pp. 225–235, 2019, doi: 10.1016/j.actbio.2019.05.014.

[7] M. Malinauskas *et al.*, “3D artificial polymeric scaffolds for stem cell growth fabricated by femtosecond laser,” *Lith. J. Phys.*, vol. 50, no. 1, pp. 75–82, 2010, doi: 10.3952/lithjphys.50121.

[8] P. Fomby *et al.*, “Stem cells and cell therapies in lung biology and diseases: Conference report,” *Ann. Am. Thorac. Soc.*, vol. 12, no. 3, pp. 181–204, 2010, doi: 10.1002/term.

[9] C. Yu *et al.*, “Biomaterials Scanningless and continuous 3D bioprinting of human tissues with decellularized extracellular matrix,” *Biomaterials*, vol. 194, no. September 2018, pp. 1–13, 2019, doi: 10.1016/j.biomaterials.2018.12.009.

[10] S. D. Gittard, A. Ovsianikov, B. N. Chichkov, A. Doraiswamy, and R. J. Narayan, “Two-photon polymerization of microneedles for transdermal drug delivery,” *Expert Opin. Drug Deliv.*, vol. 7, no. 4, pp. 513–533, 2010, doi: 10.1517/17425241003628171.

[11] S. D. Gittard *et al.*, “Fabrication of polymer microneedles using a two-photon polymerization and micromolding process,” *J. Diabetes Sci. Technol.*, vol. 3, no. 2, pp. 304–311, 2009, doi: 10.1177/193229680900300211.

[12] S. D. Gittard, A. Nguyen, K. Obata, A. Koroleva, R. J. Narayan, and B. N. Chichkov, "Fabrication of microscale medical devices by two-photon polymerization with multiple foci via a spatial light modulator," vol. 2, no. 11, pp. 267–275, 2011.

[13] J. Voldman, M. L. Gray, and M. A. Schmidt, "Microfabrication in biology and medicine," *Annu. Rev. Biomed. Eng.*, no. 1, pp. 401–425, 1999, doi: 10.1146/annurev.bioeng.1.1.401.

[14] B. Bhushan and M. Caspers, "An overview of additive manufacturing (3D printing) for microfabrication," *Microsyst. Technol.*, vol. 23, no. 4, pp. 1117–1124, 2017, doi: 10.1007/s00542-017-3342-8.

[15] R. K. Kupka, F. Bouamrane, C. Cremers, and S. Megtert, "Microfabrication : LIGA-X and applications," 2000.

[16] J. M. Park *et al.*, "Fabrication of tapered micropillars with high aspect-ratio based on deep X-ray lithography," *Materials (Basel).*, vol. 12, no. 13, 2019, doi: 10.3390/ma12132056.

[17] A. Malekabadi and C. Paoloni, "UV-LIGA microfabrication process for sub-terahertz waveguides utilizing multiple layered SU-8 photoresist," *J. Micromechanics Microengineering*, vol. 26, no. 9, 2016, doi: 10.1088/0960-1317/26/9/095010.

[18] J. D. Williams and W. Wang, "Microfabrication of an electromagnetic power relay using SU-8 based UV-LIGA technology," *Microsyst. Technol.*, vol. 10, no. 10, pp. 699–705, 2004, doi: 10.1007/s00542-004-0396-1.

[19] H. Mekaru *et al.*, "Fabrication of a spiral microcoil using a 3D-LIGA process," *Microsyst. Technol.*, vol. 13, no. 3–4, pp. 393–402, 2007, doi: 10.1007/s00542-006-0202-3.

[20] V. R. Manfrinato *et al.*, "Resolution limits of electron-beam lithography toward the atomic scale," *Nano Lett.*, vol. 13, no. 4, pp. 1555–1558, 2013, doi: 10.1021/nl304715p.

[21] Y. Chen, "Nanofabrication by electron beam lithography and its applications: A review," *Microelectron. Eng.*, vol. 135, pp. 57–72, 2015, doi: 10.1016/j.mee.2015.02.042.

[22] G. Yoon, I. Kim, S. So, J. Mun, M. Kim, and J. Rho, "Fabrication of three-dimensional suspended, interlayered and hierarchical nanostructures by accuracy-improved electron beam lithography overlay," *Sci. Rep.*, vol. 7, no. 1, pp. 1–8, 2017, doi: 10.1038/s41598-017-06833-5.

[23] D. Zhao, A. Han, and M. Qiu, "Ice lithography for 3D nanofabrication," *Sci. Bull.*, vol. 64, no. 12, pp. 865–871, 2019, doi: 10.1016/j.scib.2019.06.001.

[24] Y. Hong *et al.*, "Three-Dimensional in Situ Electron-Beam Lithography Using Water Ice," *Nano Lett.*, vol. 18, no. 8, pp. 5036–5041, 2018, doi: 10.1021/acs.nanolett.8b01857.

[25] M. Altissimo, "E-beam lithography for micro-/nanofabrication," *Biomicrofluidics*, vol. 4, no. 2, pp. 2–7, 2010, doi: 10.1063/1.3437589.

[26] J. Huang, Q. Qin, and J. Wang, “A review of stereolithography: Processes and systems,” *Processes*, vol. 8, no. 9, 2020, doi: 10.3390/PR8091138.

[27] W. Wang, J. Ye, H. Gong, X. Pi, C. Wang, and Y. Xia, “Computer-stereolithography-based laser rapid prototyping & manufacturing system,” *IFAC Proc. Vol.*, vol. 32, no. 2, pp. 61–66, 1999, doi: 10.1016/s1474-6670(17)56013-9.

[28] C. Sun, N. Fang, D. M. Wu, and X. Zhang, “Projection micro-stereolithography using digital micro-mirror dynamic mask,” *Sensors Actuators, A Phys.*, vol. 121, no. 1, pp. 113–120, 2005, doi: 10.1016/j.sna.2004.12.011.

[29] J. W. Choi, R. B. Wicker, S. H. Cho, C. S. Ha, and S. H. Lee, “Cure depth control for complex 3D microstructure fabrication in dynamic mask projection microstereolithography,” *Rapid Prototyp. J.*, vol. 15, no. 1, pp. 59–70, 2009, doi: 10.1108/13552540910925072.

[30] X. Li, H. Mao, Y. Pan, and Y. Chen, “Mask Video Projection-Based Stereolithography with Continuous Resin Flow,” *J. Manuf. Sci. Eng. Trans. ASME*, vol. 141, no. 8, pp. 1–10, 2019, doi: 10.1115/1.4043765.

[31] R. Janusziewicz, J. R. Tumbleston, A. L. Quintanilla, S. J. Mecham, and J. M. DeSimone, “Layerless fabrication with continuous liquid interface production,” *Proc. Natl. Acad. Sci. U. S. A.*, vol. 113, no. 42, pp. 11703–11708, 2016, doi: 10.1073/pnas.1605271113.

[32] J. S. Choi, H. W. Kang, I. H. Lee, T. J. Ko, and D. W. Cho, “Development of micro-stereolithography technology using a UV lamp and optical fiber,” *Int. J. Adv. Manuf. Technol.*, vol. 41, no. 3–4, pp. 281–286, 2009, doi: 10.1007/s00170-008-1461-1.

[33] D. Loterie, P. Delrot, and C. Moser, “High-resolution tomographic volumetric additive manufacturing,” *Nat. Commun.*, vol. 11, no. 1, pp. 1–6, 2020, doi: 10.1038/s41467-020-14630-4.

[34] H. Exner and A. Streek, “High resolution laser micro sintering / melting using q-switched and high brilliant laser radiation,” *Laser 3D Manuf. II*, vol. 9353, no. March 2015, p. 93530P, 2015, doi: 10.1117/12.2083777.

[35] H. Exner *et al.*, “Laser micro sintering: A new method to generate metal and ceramic parts of high resolution with sub-micrometer powder,” *Virtual Phys. Prototyp.*, vol. 3, no. 1, pp. 3–11, 2008, doi: 10.1080/17452750801907970.

[36] H. Exner, P. Regenfuss, L. Hartwig, S. Kloetzer, and R. Ebert, “Selective laser micro sintering with a novel process,” *Fourth Int. Symp. Laser Precis. Microfabr.*, vol. 5063, no. November 2003, p. 145, 2003, doi: 10.1117/12.540730.

[37] P. Regenfuss *et al.*, “Principles of laser micro sintering,” *Rapid Prototyp. J.*, vol. 13, no. 4, pp. 204–212, 2007, doi: 10.1108/13552540710776151.

[38] N. K. Roy, D. Behera, O. G. Dibua, C. S. Foong, and M. A. Cullinan, “A novel microscale selective laser sintering (μ-SLS) process for the fabrication of microelectronic parts,” *Microsystems Nanoeng.*, vol. 5, no. 1, 2019, doi: 10.1038/s41378-019-0116-8.

[39] J. P. Kruth, X. Wang, T. Laoui, and L. Froyen, “Lasers and materials in selective laser sintering,” *Assem. Autom.*, vol. 23, no. 4, pp. 357–371, 2003, doi: 10.1108/01445150310698652.

[40] H. B. Sun and S. Kawata, “Two-photon laser precision microfabrication and its applications to micro - Nano devices and systems,” *J. Light. Technol.*, vol. 21, no. 3, pp. 624–633, 2003, doi: 10.1109/JLT.2003.809564.

[41] E. T. Ritschdorff, R. Nielson, and J. B. Shear, “Multi-focal multiphoton lithography,” *Lab Chip*, vol. 12, no. 5, pp. 867–871, 2012, doi: 10.1039/c2lc21271d.

[42] Y. C. Cheng, A. Isoyan, J. Wallace, M. Khan, and F. Cerrina, “Extreme ultraviolet holographic lithography: Initial results,” *Appl. Phys. Lett.*, vol. 90, no. 2, pp. 1–4, 2007, doi: 10.1063/1.2430774.

[43] N. J. Jenness, K. D. Wulff, M. S. Johannes, M. J. Padgett, D. G. Cole, and R. L. Clark, “Three-dimensional parallel holographic micropatterning using a spatial light modulator,” *Opt. Express*, vol. 16, no. 20, p. 15942, 2008, doi: 10.1364/oe.16.015942.

[44] L. L. Yuan and P. R. Herman, “Laser scanning holographic lithography for flexible 3D fabrication of multi-scale integrated nano-structures and optical biosensors,” *Sci. Rep.*, vol. 6, no. October 2015, pp. 1–15, 2016, doi: 10.1038/srep22294.

[45] C. Slinger, C. Cameron, and M. Stanley, “Computer-generated holography as a generic display technology,” *Computer (Long. Beach. Calif).*, vol. 38, no. 8, pp. 46–53, 2005, doi: 10.1109/MC.2005.260.

[46] M. Martínez-Corral and B. Javidi, “Fundamentals of 3D imaging and displays: a tutorial on integral imaging, light-field, and plenoptic systems,” *Adv. Opt. Photonics*, vol. 10, no. 3, p. 512, 2018, doi: 10.1364/aop.10.000512.

[47] C. Hahne, A. Aggoun, V. Velisavljevic, S. Fiebig, and M. Pesch, “Refocusing distance of a standard plenoptic camera,” *Opt. Express*, vol. 24, no. 19, p. 21521, 2016, doi: 10.1364/oe.24.021521.

[48] J. Arai, H. Kawai, and F. Okano, “Microlens arrays for integral imaging system,” *NHK Lab. Note*, no. 510, pp. 9056–9078, 2007.

[49] E. H. Adelson and J. Y. A. Wang, “00121783.Pdf.” .

[50] A. Lumsdaine and T. Georgiev, “The focused plenoptic camera,” *2009 IEEE Int. Conf. Comput. Photogr. ICCP 09*, pp. 1–8, 2009, doi: 10.1109/ICCPHOT.2009.5559008.

[51] S. Zhu, A. Lai, K. Eaton, P. Jin, and L. Gao, “On the fundamental comparison between unfocused and focused light field cameras,” *Appl. Opt.*, vol. 57, no. 1, p. A1, 2018, doi: 10.1364/ao.57.0000a1.

[52] H. Zhang and S.-B. Wen, “3D photolithography through light field projections,” *Appl. Opt.*, vol. 59, no. 27, p. 8071, 2020, doi: 10.1364/ao.399508.

[53] S. Wen and H. Zhang, “HT2020- 9005,” pp. 1–7, 2020.

[54] M. B. Dickerson *et al.*, “3D Printing of Regenerated Silk Fibroin and Antibody-Containing Microstructures via Multiphoton Lithography,” *ACS Biomater. Sci. Eng.*, vol. 3, no. 9, pp. 2064–2075, 2017, doi: 10.1021/acsbiomaterials.7b00338.

[55] L. Li and J. T. Fourkas, “Multiphoton polymerization,” *Mater. Today*, vol. 10, no. 6, pp. 30–37, 2007, doi: 10.1016/S1369-7021(07)70130-X.

[56] A. Jakkinapalli, B. Baskar, and S. B. Wen, “Femtosecond two-photon 3D lightfield lithography,” *Proc. ASME 2021 Heat Transf. Summer Conf. HT 2021*, pp. 1–7, 2021, doi: 10.1115/HT2021-62290.

[57] C. Rosales-Guzmán and A. Forbes, *How to Shape Light with Spatial Light Modulators*. 2017.